ELSEVIER

Marine Geology 236 (2007) 95–119

MARINE GEOLOGY
INTERNATIONAL JOURNAL OF MARINE GEOLOGY, GEOCHEMISTRY AND GEOPHYSICS

www.elsevier.com/locate/margeo

Fe–Mn-(hydr)oxide-carbonate crusts from the Kebrit Deep, Red Sea: Precipitation at the seawater/brine redoxcline

V.M. Dekov [a,b,*], J.C. Scholten [a], R. Botz [a], C.-D. Garbe-Schönberg [a], P. Stoffers [a]

[a] *Institut für Geowissenschaften, Universität Kiel, Abt. Geologie, Olshausenstrasse-40, D-24118 Kiel, Germany*
[b] *Department of Geology and Paleontology, University of Sofia, 15 Tzar Osvoboditel Boulevard, 1000 Sofia, Bulgaria*

Received 31 January 2006; received in revised form 4 August 2006; accepted 1 October 2006

Abstract

Lithified crusts located within the sediment and recovered from the Kebrit Deep (Red Sea) are composed of Fe- and Mn-(hydr) oxides, carbonates, and sulfides. Mineralogical and geochemical features of these crusts suggest that they are metalliferous layers lithified by carbonates and formed in the narrow band where the transition zone between the anoxic brine and deep seawater crossed the seafloor. Carbonates cementing the Fe–Mn-(hydr)oxides precipitated from normal saline seawater at T=20–30 °C. Precipitation of Fe–Mn-(hydr)oxides was superimposed the carbonate precipitation in the transition zone. A pumping mechanism involving cyclic Fe- and Mn-(hydr)oxide precipitation/redissolution operated through the transition zone and produced an enrichment of a number of elements in the crusts. The microbiota played an important role in the geochemical cycle of the elements through the redoxcline and in the mineralogy of the sediments underlying the redoxcline waters. Diagenetic processes led to formation of bi- and ternary carbonates, and disulfides.

Keywords: carbonates; (hydr)oxides; sulfides; redoxcline geochemistry; Kebrit Deep; Red Sea

1. Introduction

The Red Sea is a young oceanic basin, representing a transition from continental rifting to seafloor spreading. An axial trough with a well-pronounced rift valley is developed in the southern part of the basin, whereas there is no axial rift valley in its northern part. Deeps filled with highly saline anoxic waters are distributed along the axial trough. Tectonics, hydrothermal activity and deposits of the Red Sea brine pools have been thoroughly studied during the last four decades (Degens and Ross, 1969; Bäcker and Richter, 1973; Bignell, 1975; Hartmann, 1985; Bonatti and Seyler, 1987; Izzeldin, 1987; Le Pichon and Gaullier, 1988; Missack, 1988; Blum and Puchelt, 1991; Makris and Rihm, 1991; Hartmann et al., 1998; Scholten et al., 2000; Gurvich, 2006) and this basin has become one of the best studied parts of the world ocean.

Lithified carbonate layers were described within the Red Sea sediments more than 100 years ago (Natterer, 1898). The composition, isotope geochemistry and genesis of these widespread occurrences have been discussed (Olauson, 1960; Herman, 1965; Gevirtz and Friedman, 1966; Milliman et al., 1969; Stoffers and Botz, 1990). These studies, however, describe lithified layers composed of carbonates. There are only a few reports on carbonate crusts containing laminae rich in Fe-(hydr)oxides (Veber and Gurskiy, 1982; Stoffers and

* Corresponding author. Department of Geology and Paleontology, University of Sofia, 15 Tzar Osvoboditel Boulevard, 1000 Sofia, Bulgaria.
E-mail address: dekov@gea.uni-sofia.bg (V.M. Dekov).

0025-3227/$ - see front matter © 2006 Elsevier B.V. All rights reserved.
doi:10.1016/j.margeo.2006.10.020

Botz, 1990) or sulfides (Blum and Puchelt, 1991), but none of them studied their composition in detail.

During the *R/V Meteor* cruise M31/2 (February–March 1995) a TV grab sample (# 17006-12, 24°43.6′N, 36°15.9′E, 1380 m) taken just above the Kebrit Deep seawater/brine redoxcline (Fig. 1) revealed a number of lithified sediment crusts in the soft background sediment (Hemleben et al., 1996). We report here on their composition and genesis in relation to the fluctuating seawater/brine redoxcline and hydrothermal activity.

2. Geologic setting

The Kebrit Deep, discovered during the *R/V Valdivia* cruise VA03 in 1972 (Schoell, 1974), is a single, slightly elongated, brine-filled basin about 1 by 2.5 km in size at the seawater/brine redoxcline (Fig. 1). It is a tectonically formed deep (Bonatti, 1985, 1987) with steep slopes descending about 300 m from the surrounding topographically smooth seafloor. The position of the seawater/brine transition of the 84-m-thick brine body has remained unchanged over the past 23 years (Hartmann et al., 1998). Anoxic (no O_2 has been detected) and acid (pH = 5.46–5.53) brine waters have elevated chlorinity (139.50–154.30‰ Cl) and temperature (T = 22.60–23.38 °C) compared to the ambient seawater (22.44–22.65‰ Cl, and 21.46 °C respectively) (Hartmann et al., 1998). The S content in the brine is 12–14 mg/l (Hartmann et al., 1998). The main constituents of the dissolved gases (>150 ml/l) in the brine waters are CO_2 (~42%), H_2S (16%) and CH_4 (8%) (Veber and Gurskiy, 1982). The transition zone between the ambient deep seawater and brine body is strongly layered: the upper layer relatively rich in O_2, and the lower sulfide-rich layer. The thickness of this zone recorded as temperature increase (CTD data) between the normal seawater and upper boundary of the constant brine temperature, was 7 m in 1995, and 4.5 m in 1997. According to the salinity records, the transition zone had a thickness of 1 m in 1995 (CTD data) and 2.2 m in 1997 (sound velocity sensor, SV corresponding to density and salinity) (M. Hartmann, personal communication).

The transition zone shows strong enrichment of suspended and dissolved Fe and Mn ($[Fe^{3+}]$ = 38–270 μmol/l, $[Mn^{2+}]$ = 3–173 μmol/l, $[Mn^{4+}]$ = 1–4 μmol/l; Schmidt et al., 2003) compared to the underlying brine body, implying a dynamic process of precipitation/dissolution between the oxygenated seawater and reducing brine (Hartmann et al., 1998). This maximum at the redoxcline is similar to that observed in other anoxic environments (e.g., Black Sea, Spencer and Brewer, 1971; Saanich Inlet, Emerson et al., 1979; Framvaren fjord, Skei, 1988; Bannock Basin, De Lange et al., 1990a; Orca Basin, Hurtgen et al., 1999).

Inactive sulfide chimneys (Missack, 1988; Blum and Puchelt, 1991) are situated in a narrow band nearby the

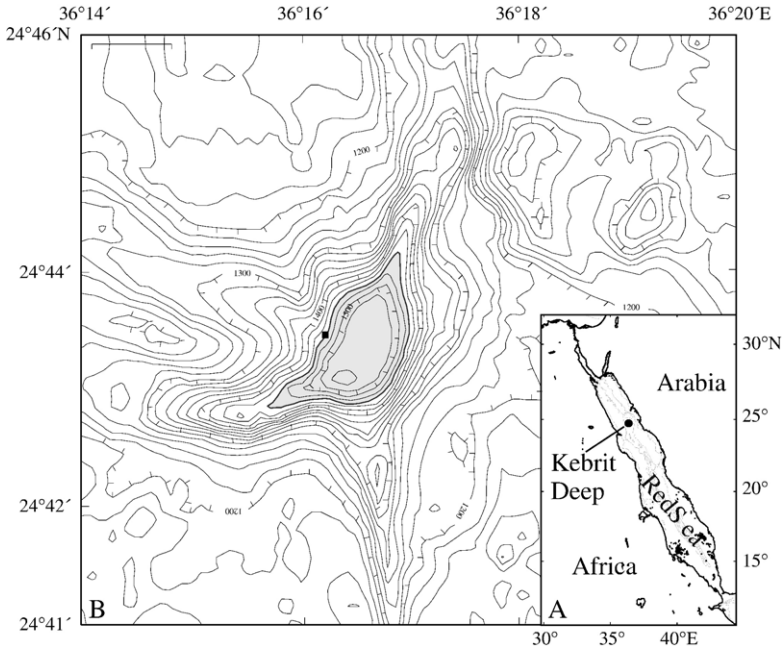

Fig. 1. (A) Overview map of the Red Sea showing the location of Kebrit Deep. (B) Bathymetric map of Kebrit Deep. Contours in meters; closed square = sampling site; shaded area = interface of the brine pool; bar in upper left is 1 km long.

Table 1
Mineralogical composition (XRD, polished and thin sections observations) of the studied crusts

Type. crust. layer	Mineralogy♠												Description
	Mg-calcite, mol% $MgCO_3$	Calcite	Aragonite	Siderite	Dolomite	Rhodochrosite	Goethite	Hematite	Lepidocrocite	Pyrite	Manganates	Quartz	
III.4.11													Light olive gray coating; soft
III.4.10	*****, 12.3	**	*	**	*		**	**			*	**	Greenish gray; soft
III.4.9	*****, 10.4			**	**		*				*	**	Light brown; hard
III.4.8	*****, 9.0			**	**		**		*		*	**	Grayish orange; soft
III.4.7	*****, 7.9			**			**	**				*	Orange; soft
III.4.6	*****, 8.7			**	**		***	***	**		*	***	Moderate reddish brown; hard
III.4.5	*****, 8.7	**		**	**		****		**			**	Dark yellowish orange with fine lamination; soft
III.4.4	*****, 9.9	*	*	*	*		*				*	**	Biogenic remnants; hard
III.4.3	*****, 9.7			**	**		**	**			*	***	Moderate reddish brown; hard; dark brown spots
III.4.2	*****, 12.3	**		**	**		**			*	*	**	Moderate yellowish brown; hard; dark green stains
III.4.1	*****, 11.3	**	*	**	*		*				*	*	White/yellowish white; hard
III.5.12										*			Whitish stains; hard
III.5.11	****, 10.4	***			**	*****	***	****	***		**	**	Black; soft
III.5.10	****, 14.6				*	*	*****	****	***		*	***	Dark reddish brown; hard
III.5.9	*****, 12.3					***	****	*****	****	*	**		Red brown; hard
III.5.8	*****, 9.9			***	**		*****		**		**	**	Dark yellowish brown; hard
III.5.7	****, 9.0	****	*			****	*****			**	*	**	Moderate yellowish brown, porous; soft
III.5.6	***, 5.5	***			*	***	*****			*	**	**	Dark yellowish brown; hard
III.5.5	***, 5.5	***			**	*****	****			*	*	**	Dark yellowish orange; soft; petroleum droplets
III.5.4		****		*	**	*****	***			*		***	Grayish orange; soft
III.5.3	**, 9.7	***			*	****	*****	**		***	*	*	Moderate brown; soft; many petroleum droplets
III.5.2	**, 8.3	**				*****	**			*		*	Dark yellowish orange; soft; petroleum droplets
III.5.1	**, 11.2	**				*****	*			*	*	*	Grayish yellow; soft; foram tests; petroleum droplets
VI.1.12	*****, 14.2	***			*	*	***		****		**	***	Grayish orange; soft
VI.1.11	***, 12.2				***		*****	**	****		**	**	Greenish black; soft
VI.1.10	***, 13.7				***		****	*****	****		****	**	Greenish brown; hard
VI.1.9	*****, 14.2			**	**		**	***	**		*	***	Moderate reddish brown; hard; dark spots
VI.1.8	*****, 13.3			*	*		*	***	*		*	**	Moderate brown; soft
VI.1.7	*****, 12.3			*	*		*	**	*			**	Grayish red; hard
VI.1.6	*****, 11.2			**	*		*	***			*	*	Moderate reddish brown; hard; homogenous
VI.1.5													Dark green lenses; hard
VI.1.4	*****, 12.6	**		**	**		*	**		*	*	**	Moderate brown; hard
VI.1.3	*****, 13.6	**		**	**		*				*	**	Light brown; hard
VI.1.2	*****, 12.6	****		**	**		**		*		*	***	Moderate yellowish brown; soft; black and green spots
VI.1.1													Black/greenish black; soft; very fine

♠Abundance codes: ***** — abundant; **** — frequent; *** − rare; ** − present; * − traces.

recent Kebrit transition zone (Scholten et al., 2000). The massive sulfides and nearby sediments, are occasionally impregnated with hydrocarbons (Veber and Gurskiy, 1982; Michaelis et al., 1990; Galimov et al., 1995).

3. Materials and methods of investigation

TV observations and sampling of the area above the transition zone and around the inactive chimney field indicated no consolidated coverings on the soft sediment, implying that the crusts that we have taken originate beneath the seawater/sediment interface. Similar crusts have been cored in the Kebrit Deep proper (Veber and Gurskiy, 1982; Michaelis et al., 1990).

The crusts exhibit fine, distinctive layering. We subdivided them into 6 lithological types after macroscopic and binocular (WILD M400) observations. Thin and polished sections were used for detailed microscopic and microprobe studies. The chemical composition of different mineral phases (point analyses) was determined by employing a Cameca microprobe (U=15 kV; I=15.6 nA; electron beam diameter of 1 μm; detection limits 0.1 wt.%). Natural standards (pyrite, goethite) were used. Scanning electron microscope (SEM) observations were made on C-coated crust fragments using a JEOL JSM-5410LV electron microscope coupled with EDS.

Each visually recognizable crust layer was carefully sampled for further analyses by a diamond mini drill.

X-ray diffraction (XRD) examinations on air-dried mounts of finely ground sample powders were made using a Phillips PW 1710 XRD system: Cu K_α radiation with a monochromator, step velocity 0.04°2Θ/s, U=40 kV, I=30 mA, angle range 5°–65°2Θ, Phillips PC-APD software. Quartz, present in all crust layers, was used as an internal standard for measuring the shift of the main mineral peaks.

All monolayer samples were air dried over silica gel at room temperature, subsequently ground in an agate mortar and re-dried prior to chemical analyses. Determinations for 36 trace elements (REE included) were made by Inductively Coupled Plasma Mass Spectrometry (ICP-MS), using a VG PlasmaQuad PQ 1 instrument, after total digestion of the samples following a pressurized HF–$HClO_4$–aqua regia decomposition procedure (Garbe-Schönberg, 1993). Analytical precision and accuracy of the data were checked with duplicate samples and certified reference materials. Details about the decomposition procedure, instrumentation and operating conditions, data acquisition and analytical quality control procedures have been published by Garbe-Schönberg (1993).

Fe and Mn were measured by AAS (Perkin Elmer Z-5000; precision <5%). The accuracy was checked using international standards (GSPN-3, Nod-P-1). The carbonate content was measured by applying the method of Müller and Gastner (1971).

Carbon- and O-isotopic composition of 6 samples was investigated by the common phosphoric acid method (e.g., reaction with 100% H_3PO_4 at 25 °C; McCrea, 1950). The samples consisted of more than 95% monomineralic Mg-calcite (samples III.4, with traces of siderite and dolomite only) and almost 100% rhodochrosite (samples III.5, with traces of Mg-calcite) (Table 1). The isotope ratios of the liberated CO_2 were measured with a MAT 251 IR-MS. The data are reported relative to the common PDB standard. Standard deviation is 0.15‰ for O and 0.1‰ for C based on replicate analysis of the standard.

Principal Component Analysis (PCA) with a varimax rotation was used with a correlation matrix generated from the geochemical data set.

4. Results

Background Kebrit sediments are composed of biogenic (foraminifera, pteropods, nannofossils) and terrigenous (quartz, feldspars, clay minerals) material.

The crusts we studied were hard, flat slabs (≤2.5 cm thick), with irregular surfaces, and composed of fine laminae (~1 mm) varying in color: white, yellow, green, red, brown, black (Fig. 2A). Crust types (crust lithology is available on request) are: (I) carbonate and carbonate-clayey crusts; (II) pitted carbonate/Fe–Mn-(hydr)oxide crusts; (III) yellow/red carbonate/Fe-(hydr)oxide crusts; (IV) ochrous/brown Fe-(hydr)oxide crusts; (V) grayish black finely laminated crust; (VI) Fe–Mn-(hydr)oxide/carbonate crusts.

We focused our research on types III and VI crusts because: (a) type I crusts are already well studied; (b)

Fig. 2. (A) Photograph of a cross section through a Fe–Mn-(hydr)oxide-carbonate crust (III.4); (B) SEM microphotograph of Fe-calcite spherule and Ca–Mg-siderite rhombohedral crystals [secondary electron image (SEI); crust III.1]; (C) EDS spectrum of the Fe-calcite spherule shown at (B); (D) EDS spectrum of the Ca–Mg-siderite crystals shown at (B); (E) SEM microphotograph of Fe-oxyhydroxide crystals encrusting the surface of bacterial filaments (SEI; crust IV.4); (F) SEM microphotograph of Mn-oxide botryoids (SEI; crust IV.1); (G) SEM microphotograph of botryoids of Mn-oxide septal crystals [SEI; enlargement of upper central part of (F)]; (H) SEM microphotograph of tar droplet (SEI; crust III.1).

types II and IV have very simple mineralogy and geochemistry (preliminary studies); (c) we had only one small crust from type V and were not able to separate enough monolayer material for studies; (d) types III and VI crusts are multilaminated and may record varying environmental conditions in the Kebrit Deep.

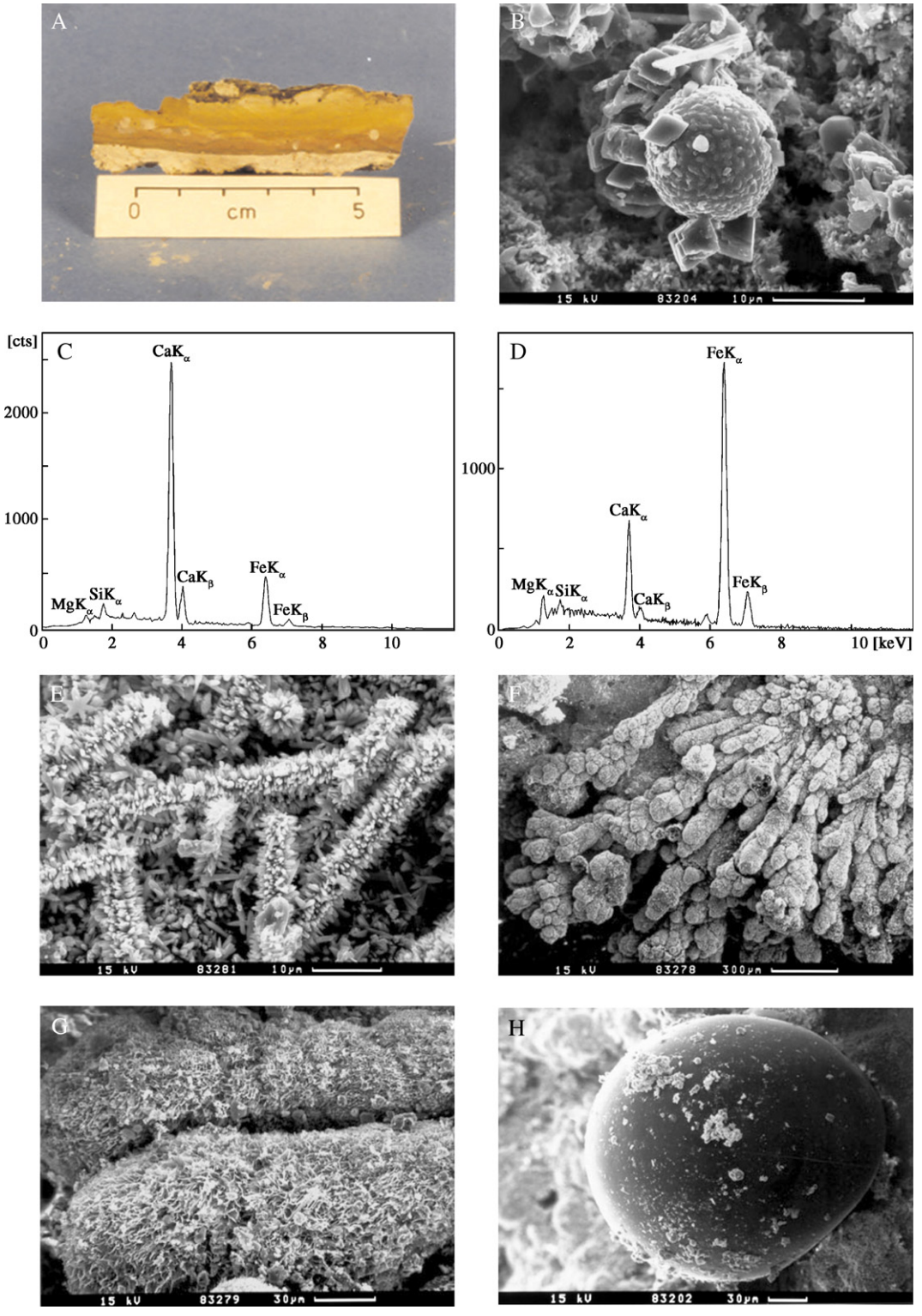

4.1. Mineralogy

With a few exceptions the main mineral of the studied crusts is high Mg-calcite (5.5–14.6 mol% $MgCO_3$, Table 1). The percentage of $MgCO_3$ in calcite crystal lattice was determined according to the position of the main calcite peak (211) (Milliman, 1974). Traces of pure calcite accompany the Mg-calcite. Microscopic studies (polished sections; SEM) revealed the calcite is biogenic: foraminiferal tests and coccoliths (Fig. 3A). Traces of aragonite (pteropod shells; microscopic observations) were found in a few layers. High Mg-calcite fills biogenic remnants scattered in homogenous micritic high Mg-calcite matrix (Fig. 3A). SEM-EDS studies revealed spherules of Fe-calcite (Fig. 2B,C).

Siderite is present in trace amounts in almost all layers of crusts III.4 and VI.1 (Table 1). SEM-EDS studies proved it is Ca–Mg-siderite (Fig. 2B,D). Traces of ankerite [$Ca(Fe, Mg)(CO_3)_2$] are present in only 3 layers (III.5.3, III.4.3, III.4.6).

"Proto-dolomite", is an accessory mineral in almost all crust layers too. Its main peak d(104) is often between the main peaks of dolomite and Mg-kutnahorite testifying for the immature nature of the mineral. In some layers of crusts III.4 and III.5, the "dolomite" peaks are closer to the peaks of ankerite suggesting for a presence of a complex ternary carbonate (Ca, Mg, Fe)CO_3.

Rhodochrosite is the main mineral in almost all layers of crust III.5 that contains tar and asphalt droplets (Table 1). It is not pure (XRD peaks deviate from the standard data) and probably contains varying proportions of Ca, Mg and Fe. Rhodochrosite forms fine homogenous rhodochrositic matrix with scattered calcitic foraminiferal tests and clastic grains (Fig. 3B). It is important to note that in many cases the small foraminiferal chambers are filled with Mn-(hydr)oxides whereas the large chambers are filled with rhodochrosite (Fig. 3B).

Goethite (α-FeOOH) is the most abundant Fe-(hydr) oxide in the Kebrit crusts (Table 1). Hematite (α-Fe_2O_3) and lepidocrocite (γ-FeOOH) are less common and occur mainly in crusts III.5 and VI.1. Lattice spacings of these minerals are enlarged probably due to incorporation of other metal cations in their crystal lattices.

Two types of goethite, primary and secondary (formed via oxidation of pyrite) were observed. Primary goethite forms isometric grains with thin, lath-like, radial crystals on their surfaces, or aggregates of finely dispersed particles (Fig. 3 B). It coats often other mineral grains (clastic components, biogenic remnants) or fills interstitial voids between them and cements the matrix.

Very fine, irregular pyrite particles are disseminated in large, isometric, porous goethite grains with sharp outlines. Rarely goethite forms zoned cubic grains pseudomorphing pyrite, and more commonly is colloform with pyrite relics. This type of goethite is a secondary phase after pyrite. In many cases, the pyrite is almost totally replaced by goethite. Goethite types differ in their chemical composition (Table 2): primary lath-/needle-like goethite is pure; finely dispersed goethite has high Si and P content; secondary goethite is enriched in S. The goethite is poorly crystalline (broad main XRD peaks). The shift in its unit cell dimensions towards those of groutite (α-MnOOH) suggests some Mn-for-Fe substitution (Stiers and Schwertmann, 1985). Calculated goethite formula is: $Fe_{0.95}Mn_{0.05}OOH - Fe_{0.97}Mn_{0.03}OOH$.

Hematite is present as dense finely flaked aggregates. Lepidocrocite occurs as elongated plates. Bacterial filaments heavily encrusted by Fe-oxyhydroxides occur often (Fig. 2E).

Weak peaks with 10 Å, 7 Å, 4.8–4.9 Å, 3.2–3.4 Å and 2.4–2.5 Å d-spacings on the XRD patterns suggest presence of traces of marine 10 Å manganates. They are sometimes unstable in air (10 Å reflections were missing) and have transformed to 7 Å manganates (Usui et al., 1989). Septal crystals of Mn-oxides form botryoids (Fig. 2F,G).

Pyrite was found in all the studied crusts. It is fairly abundant in crust III.5 rich in petroleum droplets and rare in the other crusts. There are 3 pyrite generations: framboidal or oval porous (i) (Fig. 3 C, D, F), lined by massive, fine grained, brownish, with slight anisotropism (ii) (Fig. 3 D, F) both rimmed by colloform pyrite (iii) (Fig. 3 C, F). Framboids, composed of cubic, pyrite microcrystals (Fig. 3 F), are loose aggregations or partly impregnated by pyrite matter (Fig. 3 F). They are single or form polyframboids (Fig. 3 B, D) and irregular patches (Fig. 3 A, C, E). Pyrite (ii) is the least resistant to oxidation generation, alters first (Fig. 3 F) and forms bird-eye textures (Fig. 3 C). Colloform pyrite (iii) converts to goethite second (Fig. 3 F). The most resistant to oxidation is the framboidal pyrite (i) (Fig. 3 D). Pyrite from all three generations has a composition very close to the stoichiometric values (Table 2). Two compositional trends are delineated: (1) surplus Fe in pyrite (ii) and (iii); (2) increase in Ni content from pyrite (i) to pyrite (iii) (Table 2). The first trend is likely associated with the different pyrite susceptibility to oxidation.

Traces of a rare mineral, γ-MnS, were revealed (XRD) in layer III.5.4. Terrigenous quartz (irregular, angular grains) is present in all crust layers in insignificant amounts (Table 1). Asphalt and tar droplets occur in some crust layers (Fig. 2H).

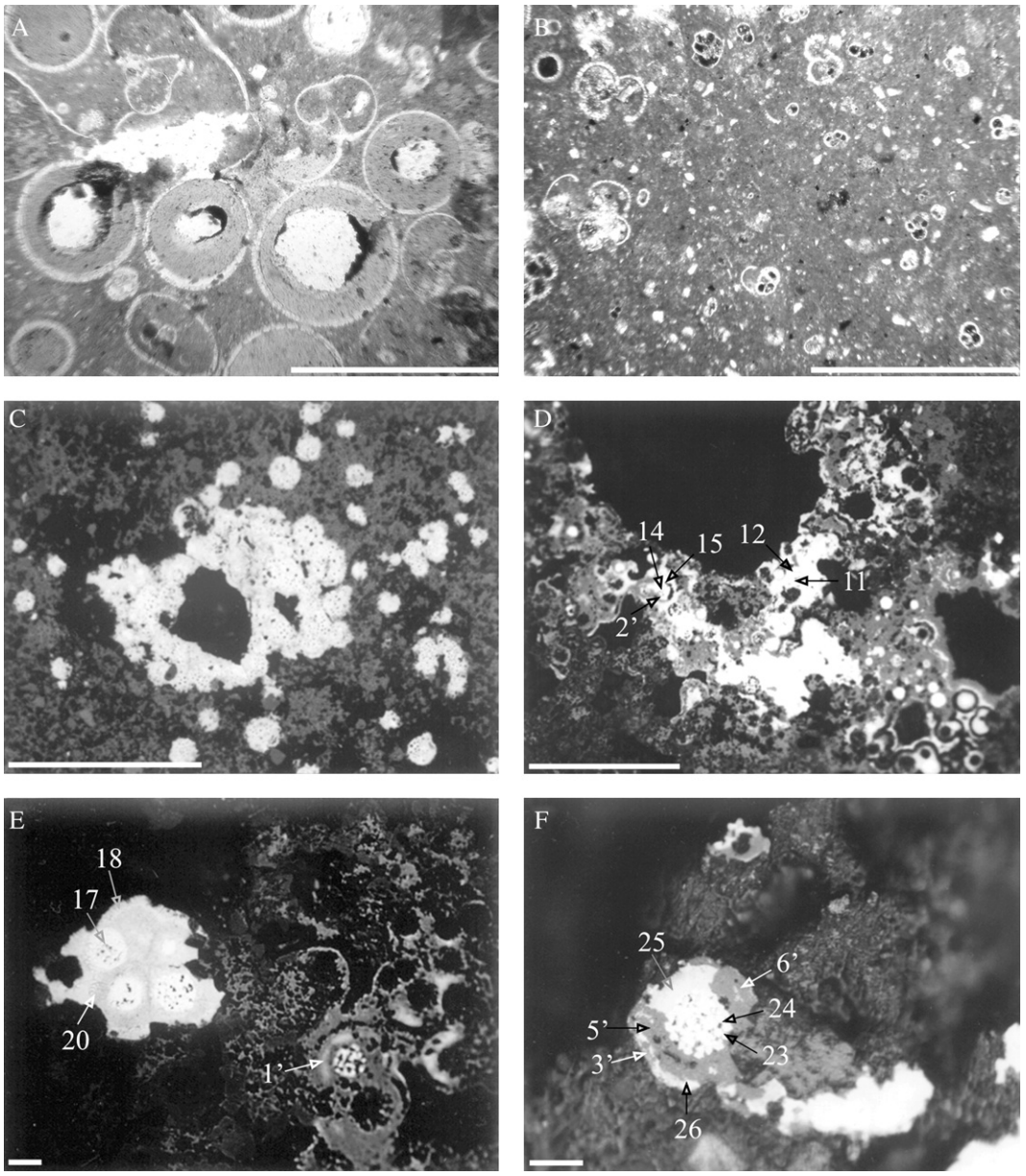

Fig. 3. Photomicrographs (air; || N) of thin (A, B) and polished (C–F) sections from Kebrit Deep Fe–Mn-(hydr)oxide-carbonate crusts. (A) Intact foraminiferal (calcite) and pteropod (aragonite) tests filled with and in homogenous micritic high-Mg calcite matrix; note the fibrous radial calcite building the foraminiferal tests (III.4). (B) Fine homogenous rhodochrosite matrix with scattered foraminiferal tests and clastic grains; note the rhodochrosite (grey) and Mn-(hydr)oxide (black) filling of the foraminiferal chambers (III.5). (C) Pyrite framboids and polyframboids (white, porous, oval) in goethite (grey) matrix (III.4). (D) Three pyrite (white) generations: (i) framboidal or globular in the centre; (ii) massive, filling the space between the globules or framboids; and (iii) colloform, rimming the massive or framboids/polyframboids; ii and iii selectively replaced by goethite (grey) (III.5.3). (E) Framboidal pyrite (white, porous, oval) rimmed by massive pyrite (greyish white); goethite (grey) replacing both massive pyrite and colloform rims of the framboidal pyrite (right side); relic of a framboid (III.5.3). (F) Big framboid; the framboidal central part with well formed cubic crystals is clearly visible; the massive part is almost replaced by goethite (grey); relics of the massive and colloform parts are still preserved (III.5.3). Arrows with numbers=microprobe analyses (Tables 2 and 3). Scale bars equal to 500 μm (A, B), 100 μm (C, D), 10 μm (E, F).

4.2. Geochemistry

Background Kebrit Deep sediments (BKDS) owe their composition to the terrigenous and biogenic input. The main biogenic component in the crusts, carbonates, contribute negligibly to the geochemical cycle of all studied elements (excluding Sr) since these elements are present in very low concentrations in the carbonates.

Hence, the main sources of studied elements (other than Ca and Sr) in the Kebrit crusts are terrigenous and hydrothermal/hydrogenous. With one exception only (III.4.1) the studied crust layers are metalliferous [(Fe+Mn)/Ti>25; Gurvich, 2006]. The carbonate content in them varies between 3.3 and 89.9% (Table 3). The excess contents of non-lithophile elements are supposed to be mainly due to the hydrothermal/hydrogenous influence. We estimated the excess of studied elements over the background values (Table 3) using: the composition of the BKDS as a comparative background matrix; and Ti as a terrigenous tracer assuming its absence in the possible hydrothermal fluids (as found in most submarine hydrothermal systems) and its zero-excess in sediments:

$$El_{ex} = El_{bulk} - El_{BKDS} \cdot (Ti_{bulk}/Ti_{BKDS}).$$

Bulk Fe content of the layers (mean 25%; range 0.59–52.2%; Table 3) usually exceeds several times that of the BKDS and sometimes reaches values as high as in the Kebrit sulfide chimneys (Blum and Puchelt, 1991). Large Fe_{ex} contents (84–99% of the bulk Fe) indicate the hydrothermal/hydrogenous input is the main source for Fe in the crusts. Vertical distribution of Fe_{ex} across the crusts' layers exhibits smooth fluctuations suggesting temporal changes in the Fe supply. We found relevant the comparison of the chemistry of studied crusts with the composition of other metalliferous layers revealed in the same basin. Site VA-3-512 (Bignell et al., 1976) cored two metalliferous horizons in the central part of the deep: 300–310 cm, rich in framboidal pyrite; and 310–370 cm, rich in Fe-(hydr)oxides. The iron contents of the studied crusts are comparable with that of the Fe-(hydr)oxide horizon of core VA-3-512 and exceed that of the VA-3-512 pyrite rich layer (Table 3).

Manganese content (mean 2.35%; range 0.10–8.70%) also exceeds that of the BKDS (Table 3) with only one exception (III.4.1). Excess-manganese is about 95% (42–99.9%) of its total concentration implying a hydrothermal/hydrogenous source. Changes in the vertical distribution of Mn_{ex} suggest fluctuations in the environmental conditions during crust formation. The excess contents of Mn and Fe correlate well (r=0.93) unlike their bulk concentrations (r=0.37; Table 4). Manganese is one order of magnitude more than that of the VA-3-512 metalliferous horizons.

The main terrigenous element, Ti (mean 509 ppm; range 50–1159 ppm), is depleted in the crust layers relative to the BKDS (Table 3) and comparable, but less than that of the metalliferous sediments cored in the deep itself. Concentrations of two other lithophile elements, Cr (mean 20.7 ppm; range 1.7–90.2 ppm) and Hf (mean 0.73 ppm; range 0.05–1.99 ppm), are less than those of the BKDS. Some crust layers are Cr- or Hf-starved relative to the theoretically calculated values; others exhibit a little excess (means 24% and 20%, respectively, from their total contents) suggesting that a part of them is hydrogenous.

The mean Cu content (30 ppm; range 4.8–74.9 ppm) is around that of the BKDS, but less than Cu concentrations of the metalliferous sediments from the central part of the deep (Table 3). Zinc (mean 290 ppm; range 39–1216 ppm) is enriched in the crusts relative to the BKDS and comparable with the Zn contents of the central deep metalliferous sediments (Table 3). Cobalt content in the crusts (mean 45 ppm; range 6.7–205 ppm) exceeds several times that of the BKDS and central deep metalliferous horizons. Correlation between these three elements is high (r>65). They are related mostly to Mn phases, then to Ti (terrigenous matter) and to a lesser extent to Fe (Table 4). A remarkable feature is the correlation (r>0.57) of the excess contents (in % from the total) of Cu, Zn and Co to the Fe_{ex} and Mn_{ex}.

Barium (mean 57.8 ppm; range 10.4–273.4 ppm), Pb (mean 19.1 ppm; range 0.29–144 ppm) and Th (mean 1.05 ppm; range 0.09–3.85 ppm) are depleted in the Kebrit crusts relative to the BKDS and metalliferous horizons of the deep proper (Table 3). Low excess levels, even deficiency, particularly for Ba and Pb, suggest high dilution by non-terrigenous sources with near-zero contribution of these elements to the crusts.

Antimony (mean 8.85 ppm; range 0.38–31.7 ppm) is enriched in the crusts relative to the BKDS (Table 3). Sb_{ex} is about 94% of its total content. Molybdenum (mean 64.9 ppm; range 2.5–194.4 ppm) is strongly enriched in the Kebrit crusts. Only one crust layer (III.4.1) has Mo concentration close to the average crustal value (Wedepohl, 1971), while all the other layers reach values as high as those of sediments of other anoxic basins (Crusius et al., 1996) even exceed them (Table 3).

Fig. 4 shows the component factor loadings produced by the geochemical data set after a varimax rotation for 3 of the 4 components with eigenvalues >1. Factor 1 (eigenvalue 26; 43.1% of total variance explained) is characterized by high positive loadings for Ti, Cr, Cu, Rb, Y, Zr, Nb, Sn, Cs, REE, Hf, Ta, and Th and no high negative loadings. Obviously this factor represents the terrigenous phase. Factor 2 (eigenvalue 4.6; 24.6% of total variance explained) shows high positive loadings for Fe, Cu, Zn, Mo, Sb, Tl, Pb, and U and a high negative loading for Sr. It is interpreted as Fe-phase factor. Factor 3 (eigenvalue 1.4; 14.4% of total variance explained) exhibits high positive loadings for Mn, Cr,

Table 2
Representative electron microprobe analyses (in wt.%) of goethite and pyrite

Type.crust. layer	Point #	Si	Al	Ti	Mg	Ca	Na	K	Fe	Mn	S	P	Cr	Ni	Cu	Zn	V	Cl	F	Total[a]	Formula	Description
III.4.11	19′	2.89	0.08	0.08	1.02	1.17	0.43	0.06	26.01	0.09	0.35	0.45	0.00	0.00	–	0.03	–	0.85	0.00	89.53	–	Fine goethite layer
III.5.1	7	–	–	n.d.[b]	–	–	–	–	45.44	0.04	51.42	–	–	0.04	n.d.	–	n.d.	–	–	96.96	$Fe_{1.009}S_{1.989}$	Colloform pyrite
	8	–	–	n.d.	–	–	–	–	45.02	n.d.	51.55	–	–	0.08	n.d.	–	n.d.	–	–	96.65	$Fe_{1.001}S_{1.997}$	Pyrite grain
III.5.3	1′	1.03	0.13	0.00	1.27	0.33	0.34	0.03	23.26	0.09	8.27	0.04	0.00	0.09	–	0.06	–	0.37	0.32	94.58	–	Goethite rim of framboidal pyrite
	2′	1.78	0.27	0.00	1.87	0.29	0.05	0.00	24.32	0.06	1.33	0.06	0.01	0.08	–	0.22	–	0.16	0.05	82.26	–	Goethite lining porous oval pyrite and lined by colloform pyrite
	3′	1.42	0.20	0.06	1.61	1.78	0.20	0.02	23.23	0.13	9.62	0.07	0.00	0.00	–	0.16	–	0.25	0.01	101.02	–	Goethite replacing outer colloform pyrite rim
	6′	1.67	0.27	0.00	1.74	0.16	0.07	0.01	24.98	0.06	3.32	0.07	0.00	0.00	–	0.08	–	0.21	0.00	88.31	–	Goethite replacing pyrite
	9	–	–	0.02	–	–	–	–	46.52	0.02	50.91	–	–	n.d.	n.d.	–	n.d.	–	–	97.49	$Fe_{1.032}S_{1.967}$	Pyrite in goethite grain
	10	–	–	0.01	–	–	–	–	45.41	n.d.	50.53	–	–	n.d.	n.d.	–	n.d.	–	–	95.95	$Fe_{1.021}S_{1.979}$	Framboidal pyrite with goethite rim
	11	–	–	0.02	–	–	–	–	44.99	0.02	52.21	–	–	0.14	n.d.	–	n.d.	–	–	97.39	$Fe_{0.992}S_{2.004}$	Porous oval pyrite grain
	12	–	–	0.01	–	–	–	–	42.64	0.03	43.56	–	–	0.33	0.01	–	0.03	–	–	86.61	$Fe_{1.076}S_{1.914}$	Brownish pyrite which rims porous oval pyrite
	13	–	–	0.01	–	–	–	–	42.17	0.01	48.77	–	–	0.42	0.01	–	0.01	–	–	91.40	$Fe_{0.992}S_{1.998}$	Outer colloform zone which rims the brownish pyrite
	14	–	–	0.01	–	–	–	–	45.22	0.04	52.67	–	–	n.d.	n.d.	–	0.02	–	–	97.96	$Fe_{0.990}S_{2.008}$	Porous pyrite in the center of an oval grain
	15	–	–	n.d.	–	–	–	–	45.25	0.05	46.68	–	–	0.27	n.d.	–	n.d.	–	–	92.27	$Fe_{1.070}S_{1.923}$	Peripheral colloform pyrite
	17	–	–	0.01	–	–	–	–	45.05	0.01	52.06	–	–	0.08	n.d.	–	n.d.	–	–	97.21	$Fe_{0.995}S_{2.003}$	Porous oval pyrite
	18	–	–	n.d.	–	–	–	–	43.65	0.03	51.23	–	–	0.09	n.d.	–	n.d.	–	–	95.01	$Fe_{0.985}S_{2.013}$	Peripheral colloform pyrite rim
	20	–	–	n.d.	–	–	–	–	43.43	n.d.	45.56	–	–	0.24	n.d.	–	0.01	–	–	89.25	$Fe_{1.059}S_{1.935}$	The area between the porous oval pyrite grains
	23	–	–	0.02	–	–	–	–	46.31	0.02	51.51	–	–	n.d.	n.d.	–	0.03	–	–	97.89	$Fe_{1.021}S_{1.977}$	Framboidal pyrite
	24	–	–	0.02	–	–	–	–	46.08	0.03	50.90	–	–	0.16	0.07	–	0.01	–	–	97.27	$Fe_{1.024}S_{1.970}$	Matter impregnating the pyrite cubes in the framboid
	25	–	–	n.d.	–	–	–	–	44.85	0.08	39.41	–	–	0.19	n.d.	–	n.d.	–	–	84.53	$Fe_{1.183}S_{1.810}$	Fine-grained pyrite rimming the framboid
	26	–	–	0.02	–	–	–	–	46.46	0.04	39.10	–	–	0.31	0.03	–	n.d.	–	–	85.96	$Fe_{1.213}S_{1.777}$	Outer colloform rim
III.5.5	8′	0.60	0.30	0.06	1.37	0.16	0.05	0.00	27.61	0.07	0.02	0.19	0.08	0.00	–	0.07	–	0.18	1.36	86.96	–	Big, isometric, porous grain
III.5.12	15′	0.12	0.01	0.03	1.25	1.27	0.03	0.01	27.74	0.01	0.12	0.03	0.00	0.01	–	0.06	–	0.03	0.00	84.15	–	Fine lath-like crystals
VI.1.4	9′	0.26	0.06	0.32	1.01	0.67	0.13	0.00	28.02	0.14	0.14	0.03	0.00	0.07	–	0.00	–	0.09	0.00	85.24	–	Isometric grain with radial crystals on the surface
	10′	0.24	0.11	0.13	1.48	1.07	0.08	0.01	28.24	0.08	0.10	0.04	0.01	0.00	–	0.04	–	0.05	0.04	86.75	–	Radial crystals
VI.1.7	11′	0.17	0.07	0.07	1.64	0.78	0.05	0.00	27.91	0.06	0.07	0.05	0.00	0.06	–	0.03	–	0.05	0.04	85.19	–	Needle-like crystals
VI.1.8	31	–	–	n.d.	–	–	–	–	46.00	0.02	44.78	–	–	0.07	0.02		n.d.	–	–	90.89	$Fe_{1.112}S_{1.885}$	Pyrite grain in goethite
VI.1.9	13′	1.27	0.15	0.06	1.54	1.34	0.30	0.02	27.45	0.22	0.12	0.19	0.01	0.00	–	0.11	–	0.39	0.06	89.28	–	Thin, long, lath-like crystal
	14′	1.04	0.08	0.05	1.01	1.14	0.41	0.03	27.54	0.13	0.21	0.19	0.01	0.10	–	0.07	–	0.67	0.00	88.25	–	Isometric goethite grain with thin, lath-like, radial crystals on the surface

[a] For goethite in oxide form.
[b] Searched for, but not detected.

Table 3
Chemical composition of the studied crusts[1]

Type. crust.layer	$CaCO_3$	Fe	Fe_{ex}	Mn	Mn_{ex}	Fe/Mn	Ti	Cr	Cr_{ex}	Co	Co_{ex}	Cu	Cu_{ex}	Zn	Zn_{ex}	Rb	Sr	Sr_{ex}	Zr	Nb	Mo	Sn	Sb	Sb_{ex}	Cs	Ba	Ba_{ex}	Pb	Pb_{ex}	U
III.4.1	89.9	.6	0	.10	.04	6.0	776	12.1	0	11.2	6.6	10.3	0	66	18	6.54	1447	1142	18.5	2.52	2.5	.43	.38	.11	.40	34.4	0	4.39	0	1.70
III.4.2	60.8	13.9	12.9	1.70	1.64	8.2	701	18.6	4.1	55.6	51.5	64.7	50.4	593	549	7.02	895	619	26.6	2.82	68.5	.54	13.1	12.8	.44	68.5	0	16.7	0	9.00
III.4.3	60.2	12.9	12.1	.77	.73	16.7	534	20.5	9.5	23.9	20.8	36.2	25.3	242	208	5.14	498	287	14.6	1.91	40.0	.38	4.67	4.48	.33	34.4	0	6.41	0	4.53
III.4.4	82.3	4.2	3.5	.45	.41	9.3	443	5.8	0	16.9	14.3	14.3	5.3	83	55	4.66	644	470	13.8	1.76	15.7	.24	1.78	1.62	.30	34.6	0	6.23	0	2.46
III.4.5	44.9	25.5	24.9	1.24	1.21	20.6	412	11.1	2.6	16.0	13.6	21.3	12.9	142	116	5.74	328	166	13.9	1.91	59.8	.24	5.74	5.59	.41	39.5	0	3.21	0	6.11
III.4.6	70.9	23.9	23.2	.97	.93	24.6	491	7.6	0	15.8	12.9	14.4	4.4	66	35	6.91	334	141	15.5	2.29	59.5	.27	7.41	7.23	.52	36.8	0	2.19	0	8.39
III.4.7	61.7	15.8	15.3	.64	.62	24.7	339	5.0	0	13.3	11.3	11.0	4.0	55	33	4.87	411	278	12.0	1.71	38.6	.24	5.58	5.46	.37	25.5	0	1.76	0	6.31
III.4.8	72.4	9.4	8.7	.57	.54	16.5	454	6.2	0	14.4	11.7	10.6	1.3	48	19	5.44	492	313	14.5	1.96	26.9	.24	3.50	3.34	.37	31.2	0	2.54	0	4.35
III.4.9	76.9	5.9	5.2	.64	.60	9.2	474	7.3	0	15.6	12.8	10.4	.7	58	28	5.51	627	441	15.5	2.04	20.2	.25	2.31	2.14	.36	36.7	0	2.32	0	3.09
III.4.10	73.7	6.0	5.2	.94	.90	6.4	514	20.5	9.9	24.1	21.0	11.3	.8	85	53	6.11	672	470	19.6	3.23	13.9	.40	1.98	1.79	.42	59.6	0	5.82	0	2.29
III.4.11	–	12.3	11.2	6.17	6.12	2.0	749	30.5	15.1	79.3	74.8	24.6	9.3	224	177	7.16	631	336	32.1	8.00	54.5	.84	5.78	5.51	.41	273	18.4	11.1	0	3.27
III.5.1	72.0	31.1	30.6	1.00	.97	31.1	335	8.3	1.4	23.4	21.4	8.3	1.5	67	46	7.57	222	90	9.5	1.37	17.0	.24	.39	.27	.58	22.4	0	4.02	0	8.43
III.5.2	49.7	37.0	36.6	.80	.78	46.3	254	5.6	.4	26.1	24.6	7.1	1.9	141	126	4.92	163	63	10.7	1.07	18.4	.17	1.51	1.42	.38	15.7	0	4.57	0	10.9
III.5.3	5.9	52.2	51.9	.20	.19	261.0	181	10.7	7.0	26.5	25.4	17.7	14.0	260	249	2.46	87	16	10.3	.80	44.5	.14	4.24	4.17	.21	10.4	0	14.0	8.69	9.16
III.5.4	69.8	41.5	39.8	.40	.31	103.7	1159	26.6	2.7	26.4	19.5	67.9	44.2	198	126	10.10	267	0	35.6	3.88	40.3	.39	2.30	1.89	.68	53.3	0	17.5	0	8.82
III.5.5	10.3	30.1	29.4	.50	.47	60.2	460	6.9	0	19.5	16.8	56.4	47.0	266	237	5.66	161	0	15.0	1.95	35.9	.25	3.24	3.07	.42	26.2	0	8.51	0	5.05
III.5.6	7.9	44.3	43.9	3.90	3.88	11.3	298	5.4	0	28.9	27.1	33.4	27.3	266	248	3.68	132	15	9.0	1.25	49.3	.17	4.01	3.90	.27	70.7	0	6.15	0	8.68
III.5.7	13.7	42.5	42.1	2.40	2.38	17.7	238	13.7	8.8	25.3	23.9	30.2	25.3	185	171	2.94	154	60	7.6	.94	46.9	.15	3.13	3.04	.20	51.1	0	3.42	0	6.81
III.5.8	24.5	36.2	35.9	4.10	4.08	8.8	230	6.1	1.4	31.2	29.8	27.1	22.4	170	156	2.65	242	152	7.4	.88	56.8	.15	6.97	6.89	.18	71.5	0	2.76	0	6.01
III.5.9	17.9	44.1	43.8	5.00	4.99	8.8	187	10.9	7.0	45.9	44.8	25.9	22.1	321	309	1.98	260	187	11.5	.96	127.0	.18	20.3	20.2	.14	54.2	0	10.7	5.19	16.5
III.5.10	6.7	43.6	42.9	3.60	3.57	12.1	473	26.3	16.5	92.9	90.1	40.8	31.1	819	790	2.36	216	30	31.3	3.00	155.0	.43	24.3	24.1	.15	42.1	0	44.7	30.8	20.7
III.5.11	–	38.6	37.1	4.60	4.53	8.4	978	90.2	70.0	205.0	199.2	50.3	30.3	1216	1155	4.31	291	0	54.8	10.39	179.0	1.11	22.4	22.0	.30	78.1	0	144	115	17.9
III.5.12	–	5.2	4.4	.60	.56	8.7	544	19.0	7.8	25.2	22.0	10.5	0	130	95	5.19	780	566	22.5	2.74	20.5	.30	1.87	1.67	.35	31.0	0	15.2	0	2.92
VI.1.1	–	21.8	20.2	8.70	8.62	2.5	1054	76.6	54.8	191.1	184.9	74.9	53.3	409	343	8.38	441	26	52.1	16.39	99.9	1.39	14.5	14.1	.54	261	0	68.8	37.8	13.4
VI.1.2	56.6	14.9	14.0	2.65	2.61	5.6	606	12.0	0	33.0	29.4	35.5	23.1	218	181	6.45	585	346	29.4	3.71	50.2	.42	9.48	9.26	.45	77.3	0	13.8	0	7.02
VI.1.3	71.4	9.6	8.9	.96	.92	10.0	469	21.3	11.6	18.1	15.3	16.6	7.1	113	83	5.15	643	459	17.5	2.07	28.6	.25	4.86	4.69	.31	41.1	0	4.20	0	4.01
VI.1.4	60.1	17.4	16.9	1.42	1.39	12.3	356	6.1	0	16.8	14.7	8.9	1.6	79	57	4.25	529	389	12.0	1.60	47.0	.49	9.75	9.63	.30	38.2	0	2.15	0	6.98
VI.1.5	–	20.8	20.8	3.82	3.81	5.4	50	1.7	.7	6.7	6.4	4.8	3.8	39	36	.63	77	57	2.0	.20	9.2	.02	1.62	1.60	.04	15.8	0	.29	0	1.00
VI.1.6	49.1	26.6	26.2	1.26	1.24	21.1	241	10.2	5.3	15.3	13.9	9.4	4.4	71	56	3.32	426	331	8.4	1.17	65.5	.19	11.3	11.2	.25	43.5	0	1.73	0	10.2
VI.1.7	53.4	17.5	16.9	1.21	1.18	14.5	377	15.1	7.3	21.9	19.7	31.7	24.0	174	150	3.65	524	376	10.7	1.41	51.9	.20	8.54	8.41	.23	38.6	0	5.61	0	8.61
VI.1.8	56.2	22.8	22.2	1.09	1.06	20.9	416	9.4	.8	29.6	27.2	29.4	20.9	238	212	3.99	534	370	13.2	1.48	70.5	.19	11.3	11.2	.24	37.1	0	4.95	0	9.08
VI.1.9	29.0	33.2	32.4	2.95	2.91	11.3	534	22.6	11.6	60.5	57.3	42.8	31.9	555	521	5.26	376	165	36.9	2.42	123.0	.41	21.7	21.5	.34	54.6	0	17.2	1.46	12.0
VI.1.10	3.3	40.9	39.8	6.91	6.85	5.9	690	48.9	34.6	95.6	91.5	74.7	60.6	996	953	6.30	203	0	57.1	6.22	162.0	1.18	31.7	31.5	.42	79.3	0	59.9	39.7	18.2
VI.1.11	–	41.1	39.6	5.99	5.92	6.9	1011	80.9	60.0	166.5	160.5	69.1	48.5	963	900	6.90	197	0	61.8	17.35	194.0	1.51	22.5	22.1	.46	85.4	0	106	76.6	14.4
VI.1.12	26.1	32.8	31.6	3.91	3.85	8.4	797	44.1	27.7	64.8	60.1	44.7	28.5	609	559	7.60	375	61	48.0	5.15	179.0	.75	16.0	15.7	.51	51.2	0	43.9	20.5	9.80
BKDS[2]		2.4		.12		20.0	1600	33.0		9.5		32.7		100		–	630		–	–	–	–	.57		–	545		47		–
VA-3-512 Py[3]		5.7		.20		28.5	–	–		12		60		350		–	–		–	–	–	–	–		–	–		100		–
VA-3-512 Hy[4]		30.8		.17		181.2	900	–		5		340		1010		–	2600		–	–	–	–	–		–	150		80		–

Type. crust. layer	Th	Th_{ex}	Y	La	La_{ex}	Ce	Ce_{ex}	(Ce/Ce∗)[5]	Pr	Nd	Sm	Sm_{ex}	Eu	Eu_{ex}	(Eu/Eu∗)[6]	Gd	Tb	Dy	Ho	Er	Tm	Yb	Lu	ΣREE	La_N/Lu_N	Hf	Hf_{ex}	Ta	Tl	Bi
III.4.1	.66	0	3.50	4.14	0	8.65	0	.99	1.06	3.95	.88	0	.20	0	.70	.85	.12	.74	.15	.42	.06	.41	.06	21.67	7.39	.61	0	.24	.12	.04
III.4.2	.56	0	6.88	5.59	.33	12.2	.39	1.03	1.42	5.56	1.22	0	.30	.03	.70	1.39	.20	1.25	.27	.76	.12	.78	.12	31.14	4.99	.84	.14	.28	2.26	.08
III.4.3	.74	0	2.69	3.14	0	6.82	0	1.02	.81	3.03	.65	0	.15	0	.70	.64	.09	.57	.11	.32	.05	.31	.05	16.75	6.73	.49	0	.18	.42	.03
III.4.4	.43	0	2.28	3.18	0	6.90	0	1.02	.82	3.17	.66	0	.14	0	.64	.66	.10	.62	.12	.34	.05	.35	.05	17.14	6.82	.59	.15	.21	.19	.03
III.4.5	.97	.32	2.67	3.56	.47	7.92	.99	1.05	.92	3.54	.73	0	.17	.01	.71	.72	.11	.63	.13	.33	.05	.34	.05	19.17	7.63	.51	.10	.21	.75	.03
III.4.6	.92	.14	2.84	4.39	.71	9.49	1.25	1.04	1.08	4.17	.93	0	.19	.01	.63	.88	.12	.73	.14	.38	.06	.38	.06	23.00	7.84	.60	.11	.25	1.06	.04
III.4.7	.28	0	1.91	3.10	.55	6.70	1.00	1.03	.78	3.11	.66	0	.14	.01	.68	.58	.09	.53	.10	.30	.04	.27	.04	16.45	8.31	.47	.13	.21	.74	.02
III.4.8	.51	0	2.39	3.52	.12	7.72	.09	1.03	.91	3.57	.72	0	.17	0	.69	.77	.11	.67	.13	.36	.05	.36	.05	19.11	7.54	.62	.16	.23	.65	.02
III.4.9	.47	0	3.03	3.71	.15	7.86	0	.99	.98	3.81	.82	0	.19	.01	.71	.80	.12	.74	.15	.41	.06	.43	.06	20.11	6.63	.59	.11	.22	.45	.03
III.4.10	.88	.06	6.31	4.97	1.11	9.91	1.27	.91	1.38	5.54	1.25	.25	.30	.11	.72	1.27	.21	1.34	.28	.78	.12	.76	.12	28.22	4.44	.78	.27	.25	.14	.06
III.4.11	1.41	.22	7.66	5.44	0	13.1	.49	1.09	1.55	5.87	1.41	0	.36	.08	.77	1.43	.23	1.37	.28	.78	.11	.74	.11	32.77	5.30	.83	.08	.21	.26	.10
III.5.1	.96	.42	2.75	3.46	.94	9.03	3.39	1.23	.90	3.51	.81	.16	.18	.05	.70	.73	.10	.57	.11	.28	.04	.25	.04	19.99	9.27	.27	0	.12	.91	.02
III.5.2	.62	.21	2.15	2.26	.36	5.44	1.17	1.14	.58	2.26	.48	0	.12	.02	.77	.46	.07	.40	.08	.21	.03	.20	.03	12.62	8.07	.22	0	.08	.35	.01
III.5.3	.59	.31	2.17	2.32	.96	5.60	2.56	1.14	.60	2.43	.49	.14	.14	.07	.86	.50	.08	.48	.09	.26	.03	.24	.04	13.31	6.22	.31	.13	.09	1.14	.01
III.5.4	2.04	.20	5.63	6.75	0	14.1	0	.98	1.75	6.77	1.49	0	.39	0	.79	1.48	.22	1.30	.26	.73	.11	.74	.11	36.19	6.58	1.31	.15	.36	.90	.14
III.5.5	1.07	.34	3.58	4.43	.98	9.55	1.82	1.02	1.12	4.49	.96	.07	.28	.10	.88	.96	.14	.84	.17	.45	.06	.42	.06	23.94	7.91	.53	.07	.19	.15	.15
III.5.6	.66	.19	2.51	3.34	1.11	7.24	2.23	1.03	.84	3.26	.65	.07	.20	.09	.91	.69	.10	.58	.11	.29	.04	.26	.04	17.65	8.95	.31	.01	.13	.08	.11
III.5.7	.46	.08	2.09	2.54	.76	5.35	1.35	1.03	.59	2.34	.45	0	.15	.06	.96	.50	.07	.40	.08	.20	.03	.18	.03	12.91	9.07	.20	0	.09	.07	.07
III.5.8	.34	0	1.86	2.31	.59	4.35	.49	.95	.49	1.87	.40	0	.11	.03	.83	.40	.06	.31	.06	.16	.02	.16	.02	10.73	12.38	.19	0	.08	.22	.05
III.5.9	.52	.22	2.21	2.39	.98	5.76	2.62	1.18	.56	2.29	.44	.08	.13	.06	.84	.51	.07	.47	.09	.27	.04	.28	.04	13.34	6.40	.37	.18	.09	1.92	.07
III.5.10	1.26	.51	4.45	4.74	1.19	14.8	6.86	1.50	1.17	4.72	.98	.06	.24	.06	.71	1.06	.17	1.00	.21	.59	.09	.61	.10	30.49	5.08	.99	.52	.17	1.78	.28
III.5.11	3.11	1.55	7.35	7.13	0	29.0	12.6	1.88	1.92	7.52	1.81	0	.42	.05	.69	1.86	.30	1.87	.38	1.08	.17	1.14	.17	54.77	4.49	1.99	1.01	.42	1.92	1.28
III.5.12	.96	.09	4.48	4.57	.49	10.5	1.31	1.08	1.19	4.73	1.03	0	.22	.01	.63	1.07	.16	1.00	.21	.60	.09	.62	.09	26.03	5.44	.90	.35	.25	.24	.14
VI.1.1	3.85	2.17	10.5	8.52	.62	29.6	11.9	1.51	2.68	10.9	2.64	.60	.64	.24	.71	2.80	.46	2.75	.55	1.53	.23	1.49	.22	64.96	4.15	1.94	.89	.47	1.68	.97
VI.1.2	1.65	.68	8.59	6.12	1.57	14.1	3.95	1.02	1.82	7.58	1.73	.56	.45	.22	.73	2.02	.31	1.93	.40	1.15	.17	1.11	.17	39.08	3.86	1.09	.49	.28	.93	.12
VI.1.3	.34	0	3.94	3.91	.39	8.11	.22	.97	1.04	4.20	.96	.05	.22	.04	.70	.94	.15	.91	.20	.56	.08	.57	.09	21.94	4.66	.69	.22	.26	.53	.04
VI.1.4	1.49	.92	2.63	3.10	.43	6.86	.88	1.04	.81	3.13	.64	0	.15	.01	.70	.65	.10	.59	.12	.33	.05	.33	.05	16.91	6.64	.49	.13	.18	1.08	.02
VI.1.5	.09	.01	.49	.42	.05	.85	.01	.98	.10	.39	.08	0	.02	0	.76	.08	.01	.08	.02	.05	.01	.04	.01	2.15	4.50	.05	0	.02	.20	.01
VI.1.6	.49	.11	1.65	2.29	.48	5.13	1.07	1.07	.57	2.25	.43	0	.10	.01	.68	.46	.07	.40	.08	.22	.03	.21	.03	12.28	8.18	.32	.07	.13	1.53	.02
VI.1.7	.14	0	1.76	2.50	0	5.27	0	.98	.66	2.55	.56	0	.12	0	.67	.51	.07	.49	.09	.26	.04	.25	.04	13.41	6.70	.45	.07	.17	.83	.02
VI.1.8	.29	0	2.77	2.69	0	5.65	0	1.00	.67	2.61	.56	0	.13	0	.70	.56	.08	.49	.10	.29	.04	.30	.05	14.23	5.77	.38	0	.16	.49	.01
VI.1.9	1.00	.15	7.93	5.19	1.19	11.2	2.18	1.02	1.32	5.32	1.17	.13	.29	.09	.72	1.29	.20	1.34	.29	.84	.13	.86	.13	29.51	4.28	.91	.37	.19	1.15	.09
VI.1.10	1.69	.59	9.74	7.44	2.27	26.2	14.6	1.61	2.07	8.33	1.95	.62	.48	.21	.72	2.12	.34	2.07	.43	1.18	.18	1.20	.18	54.19	4.43	1.53	.84	.24	2.65	.46
VI.1.11	3.72	2.10	9.53	8.22	.64	42.1	25.1	2.33	2.31	9.34	2.11	.15	.50	.11	.69	2.33	.36	2.19	.44	1.22	.19	1.23	.19	72.71	4.64	1.72	.71	.42	2.68	1.52
VI.1.12	1.70	.43	10.0	6.88	.91	23.3	9.86	1.55	1.91	7.74	1.76	.21	.43	.13	.71	1.92	.31	1.93	.40	1.12	.17	1.17	.17	49.17	4.34	1.36	.56	.26	.95	.32
BKDS[2]	2.55		–	12		26.9			–	–	3.1		.61			–	–	–	–	–	–	–	–			1.6		–	–	–

[1]$CaCO_3$, Fe and Mn in wt.%; all the rest in ppm.

[2]Data from Bignell et al. (1976), Lissitzyn and Bogdanov (1986); Ce, Sm and Eu data are background Red Sea sediment values from Gurvich (2006).

[3]Pyrite rich horizon 300–310 cm of core VA-3-512 (Bignell et al., 1976).

[4]Fe-(hydr)oxide rich horizon 310–370 cm of core VA-3-512 (Bignell et al., 1976).

[5]$Ce/Ce^* = 2Ce_N/(La_N + Pr_N)$.

[6]$Eu/Eu^* = 2Eu_N/(Sm_N + Gd_N)$.

Table 4
Correlation coefficient matrix (Pearson) for all compositional data of Kebrit Deep Fe–Mn-(hydr)oxide-carbonate crusts (n=41)

	Fe	Mn	Ti	Cr	Co	Cu	Zn	Rb	Sr	Y	Zr	Nb
Mn	0.37											
Ti	−0.06	0.35										
Cr	0.25	0.67	0.77									
Co	0.33	0.77	0.65	0.95								
Cu	0.41	0.57	0.69	0.69	0.67							
Zn	0.49	0.61	0.53	0.8	0.82	0.73						
Rb	−0.22	0.04	0.78	0.36	0.23	0.42	0.09					
Sr	−0.8	−0.3	0.28	−0.09	−0.17	−0.2	−0.25	0.31				
Y	0.08	0.62	0.79	0.77	0.72	0.71	0.67	0.62	0.1			
Zr	0.21	0.64	0.85	0.9	0.84	0.76	0.82	0.53	−0.01	0.93		
Nb	0.11	0.7	0.77	0.91	0.89	0.63	0.61	0.47	−0.03	0.77	0.84	
Mo	0.55	0.67	0.44	0.74	0.77	0.65	0.9	0.05	−0.32	0.63	0.77	0.6
Sn	0.12	0.72	0.79	0.92	0.89	0.69	0.73	0.49	0.02	0.85	0.92	0.94
Sb	0.45	0.66	0.33	0.63	0.69	0.62	0.86	−0.03	−0.23	0.59	0.71	0.49
Cs	−0.13	−0.02	0.69	0.3	0.17	0.36	0.05	0.98	0.18	0.54	0.46	0.41
Ba	−0.05	0.73	0.51	0.53	0.6	0.42	0.23	0.37	0.09	0.59	0.5	0.68
La	0.08	0.52	0.91	0.81	0.74	0.76	0.67	0.73	0.1	0.94	0.94	0.82
Ce	0.25	0.65	0.79	0.93	0.88	0.73	0.79	0.49	−0.09	0.85	0.95	0.92
Pr	0.05	0.56	0.9	0.83	0.76	0.74	0.63	0.72	0.1	0.95	0.93	0.85
Nd	0.06	0.57	0.88	0.82	0.76	0.74	0.63	0.7	0.08	0.95	0.93	0.85
Sm	0.05	0.59	0.88	0.83	0.77	0.73	0.63	0.69	0.09	0.95	0.93	0.86
Eu	0.12	0.62	0.85	0.81	0.76	0.77	0.63	0.67	0.03	0.95	0.91	0.84
Gd	0.07	0.61	0.85	0.83	0.77	0.75	0.65	0.66	0.07	0.96	0.93	0.85
Tb	0.07	0.64	0.84	0.84	0.79	0.73	0.65	0.63	0.06	0.96	0.93	0.86
Dy	0.06	0.63	0.83	0.84	0.78	0.73	0.66	0.62	0.07	0.97	0.93	0.85
Ho	0.05	0.62	0.82	0.83	0.77	0.72	0.66	0.61	0.09	0.98	0.93	0.83
Er	0.05	0.61	0.82	0.82	0.77	0.72	0.66	0.6	0.1	0.98	0.93	0.82
Tm	0.05	0.61	0.83	0.83	0.77	0.72	0.68	0.6	0.1	0.98	0.94	0.82
Yb	0.05	0.6	0.83	0.83	0.77	0.72	0.69	0.6	0.1	0.98	0.95	0.81
Lu	0.05	0.59	0.83	0.83	0.78	0.72	0.7	0.59	0.11	0.98	0.95	0.81
ΣREE	0.17	0.63	0.85	0.9	0.85	0.75	0.74	0.6	−0.01	0.92	0.97	0.91
Ce/Ce*	0.45	0.62	0.51	0.85	0.84	0.55	0.83	0.15	−0.31	0.58	0.78	0.79
Eu/Eu*	0.56	0.16	−0.32	−0.21	−0.13	0.12	−0.07	−0.33	−0.48	−0.21	−0.27	−0.22
Hf	0.1	0.56	0.89	0.91	0.84	0.73	0.74	0.56	0.06	0.88	0.96	0.85
Ta	−0.16	0.31	0.91	0.77	0.68	0.6	0.48	0.69	0.27	0.74	0.79	0.81
Tl	0.41	0.51	0.39	0.61	0.65	0.6	0.75	0.15	−0.19	0.52	0.65	0.54
Pb	0.36	0.61	0.65	0.94	0.93	0.63	0.88	0.19	−0.19	0.66	0.85	0.81
Bi	0.3	0.64	0.66	0.94	0.92	0.63	0.77	0.25	−0.19	0.64	0.81	0.91
Th	0.26	0.62	0.79	0.89	0.87	0.67	0.64	0.51	−0.14	0.77	0.85	0.92
U	0.71	0.55	0.25	0.56	0.67	0.57	0.79	−0.05	−0.45	0.4	0.57	0.41

Co, Nb, Sn, Ba, Ce, Pb, Bi, and Th and no high negative loadings. This factor represents the Mn-phase. Factor 4 (eigenvalue 1.2; 5.3% of total variance explained) shows a high positive loading for Sr only and a high negative loading for Fe. We interpret this factor as biogenic-carbonate. Together, these 4 components account for 87.4% of the variance in the data set.

Rare earth elements (REE) and Y concentrations of the Kebrit crusts show little vertical (across the crusts) variations (Table 3). These elements are associated mainly with the terrigenous matter and to a lesser extent with the Mn-phase component (Table 4; Fig. 4). They generally show either no or a little (11–14%) excess values. Chondrite normalized REE distribution patterns (Fig. 5) show some similarities with positive or no Ce anomaly, negative Eu anomaly, LREE enrichment, flat HREE distribution (Table 3).

4.3. Oxygen and carbon isotopes

The $\delta^{18}O$ values of the carbonate crusts range between 1.2‰ (Mg-calcite) and 3.1‰ (rhodochrosite) (Table 5). The C isotope values are also different for the Mg-calcite ($\delta^{13}C$ between 2.4 and 2.9‰) and

Mo	Sn	Sb	Cs	Ba	La	Ce	Pr	Nd	Sm	Eu	Gd	Dy
0.69												
0.93	0.63											
0.03	0.42	−0.07										
0.26	0.63	0.24	0.27									
0.61	0.87	0.53	0.67	0.54								
0.76	0.95	0.65	0.46	0.47	0.9							
0.58	0.89	0.51	0.66	0.59	0.99	0.9						
0.59	0.88	0.52	0.64	0.59	0.99	0.91	1					
0.57	0.89	0.51	0.64	0.61	0.98	0.9	1	1				
0.58	0.87	0.51	0.61	0.64	0.97	0.88	0.99	0.99	0.99			
0.6	0.89	0.55	0.6	0.61	0.97	0.9	0.99	0.99	0.99	0.99		
0.61	0.9	0.56	0.57	0.63	0.96	0.9	0.99	0.99	0.99	0.99	1	
0.62	0.89	0.57	0.56	0.61	0.96	0.9	0.98	0.99	0.99	0.98	1	
0.62	0.88	0.57	0.55	0.6	0.96	0.89	0.98	0.98	0.99	0.98	0.99	1
0.62	0.87	0.58	0.53	0.59	0.96	0.88	0.97	0.98	0.98	0.98	0.99	1
0.63	0.88	0.6	0.53	0.57	0.96	0.89	0.97	0.98	0.98	0.97	0.99	0.99
0.64	0.87	0.6	0.53	0.56	0.96	0.89	0.97	0.98	0.98	0.97	0.99	0.99
0.65	0.87	0.61	0.51	0.55	0.96	0.88	0.97	0.97	0.97	0.96	0.98	0.99
0.7	0.94	0.61	0.55	0.54	0.97	0.98	0.97	0.97	0.97	0.95	0.97	0.96
0.83	0.81	0.69	0.15	0.25	0.63	0.89	0.63	0.63	0.63	0.6	0.64	0.64
−0.08	−0.27	−0.15	−0.3	0.06	−0.26	−0.25	−0.26	−0.26	−0.26	−0.13	−0.24	−0.25
0.68	0.89	0.61	0.5	0.5	0.95	0.92	0.95	0.95	0.95	0.92	0.94	0.94
0.41	0.78	0.33	0.63	0.46	0.88	0.8	0.89	0.88	0.87	0.83	0.85	0.84
0.77	0.65	0.84	0.15	0.19	0.55	0.67	0.53	0.54	0.53	0.51	0.56	0.55
0.79	0.83	0.68	0.16	0.34	0.72	0.89	0.72	0.72	0.72	0.7	0.72	0.73
0.71	0.87	0.58	0.22	0.41	0.72	0.92	0.73	0.73	0.74	0.71	0.74	0.74
0.62	0.89	0.5	0.5	0.56	0.85	0.91	0.87	0.87	0.87	0.87	0.87	0.86
0.83	0.49	0.86	−0.02	0.15	0.43	0.56	0.4	0.41	0.4	0.41	0.42	0.43

(continued on next page)

rhodochrosite ($\delta^{13}C = -1.0$ and -1.8‰, respectively) samples. These values are similar to the range of values measured earlier for carbonate crusts in the Red Sea (Stoffers and Botz, 1990).

5. Discussion

Metalliferous sediments similar to those found in other Red Sea deeps have not been observed in the Kebrit. Soft, thin, red laminae have been cored in the central part of the deep at only a few sites (Bignell et al., 1976). These occurrences along with the high Fe^{2+} and Mn^{2+} enrichment of the transition zone suggest hydrothermal activity in the Kebrit Deep and hydrothermal supply of Fe_{ex} and Mn_{ex}. The geochemical processes across the oxic/anoxic interfaces of anoxic hypersaline basins similar in origin to the Kebrit (Bannock and Tyro Basins, eastern Mediterranean) are, in general, similar: recycling of Fe and Mn resulting in enrichment of Fe, Mn and a number of minor and micro elements at the redox interface. However, the background sedimentation at the eastern Mediterranean anoxic basins is able to support Fe and Mn enrichment ([Fe] < 1 μmol/l, [Mn] = 0.5–6 μmol/l; De Lange et al.,

Table 4 (*continued*)

Ho	Er	Tm	Yb	Lu	ΣREE	Ce/Ce*	Eu/Eu*	Hf	Ta	Tl	Pb	Bi	Th
1													
1	1												
1	1	1											
0.99	1	1	1										
0.96	0.95	0.95	0.95	0.95									
0.62	0.62	0.63	0.63	0.63	0.79								
−0.25	−0.26	−0.28	−0.28	−0.29	−0.26	−0.18							
0.94	0.94	0.94	0.95	0.95	0.96	0.71	−0.33						
0.83	0.83	0.83	0.83	0.83	0.86	0.53	−0.43	0.9					
0.55	0.55	0.56	0.56	0.57	0.63	0.71	−0.27	0.6	0.44				
0.72	0.72	0.73	0.74	0.74	0.83	0.91	−0.18	0.85	0.68	0.66			
0.72	0.71	0.72	0.72	0.72	0.85	0.91	−0.16	0.82	0.73	0.61	0.95		
0.84	0.83	0.83	0.83	0.83	0.91	0.78	−0.16	0.89	0.81	0.56	0.83	0.89	
0.42	0.42	0.43	0.44	0.45	0.5	0.69	0.01	0.5	0.24	0.81	0.66	0.55	0.5

1990b) orders of magnitude lower than that detected at the Kebrit seawater/brine redoxcline ($[Fe^{3+}]$=38–270 μmol/l, $[Mn^{2+}]$=3–173 μmol/l; Schmidt et al., 2003). Obviously, the background sedimentation alone cannot account for the observed enrichment in Fe and Mn at the Kebrit redoxcline, which suggests an additional hydrothermal source of Fe and Mn. Further, the anoxic brine waters act as storage for the dissolved hydrothermal Fe^{2+} and Mn^{2+} and provide high Fe–Mn flux upward through the transition zone. It is obvious that the studied Fe–Mn-(hydr)oxide-carbonate crusts are not result of normal background sedimentation. They can be regarded as metalliferous layers lithified by carbonates.

5.1. Carbonates

Red Sea carbonates are of both biogenic and abiogenic origin. It has been estimated (Milliman et al., 1969) that more than half of the deep-sea carbonates in the Red Sea precipitated inorganically from seawater. Accordingly, primary precipitated carbonates together with diagenetic carbonates dominate the mineralogy of the Red Sea carbonate crusts (Stoffers and Botz, 1990). High Mg-calcite in the Red Sea crusts is believed to be mainly of abiogenic origin (Milliman et al., 1969). Kebrit crust high Mg-calcite is homogenous micrite (Fig. 3A). Calcitic and aragonitic

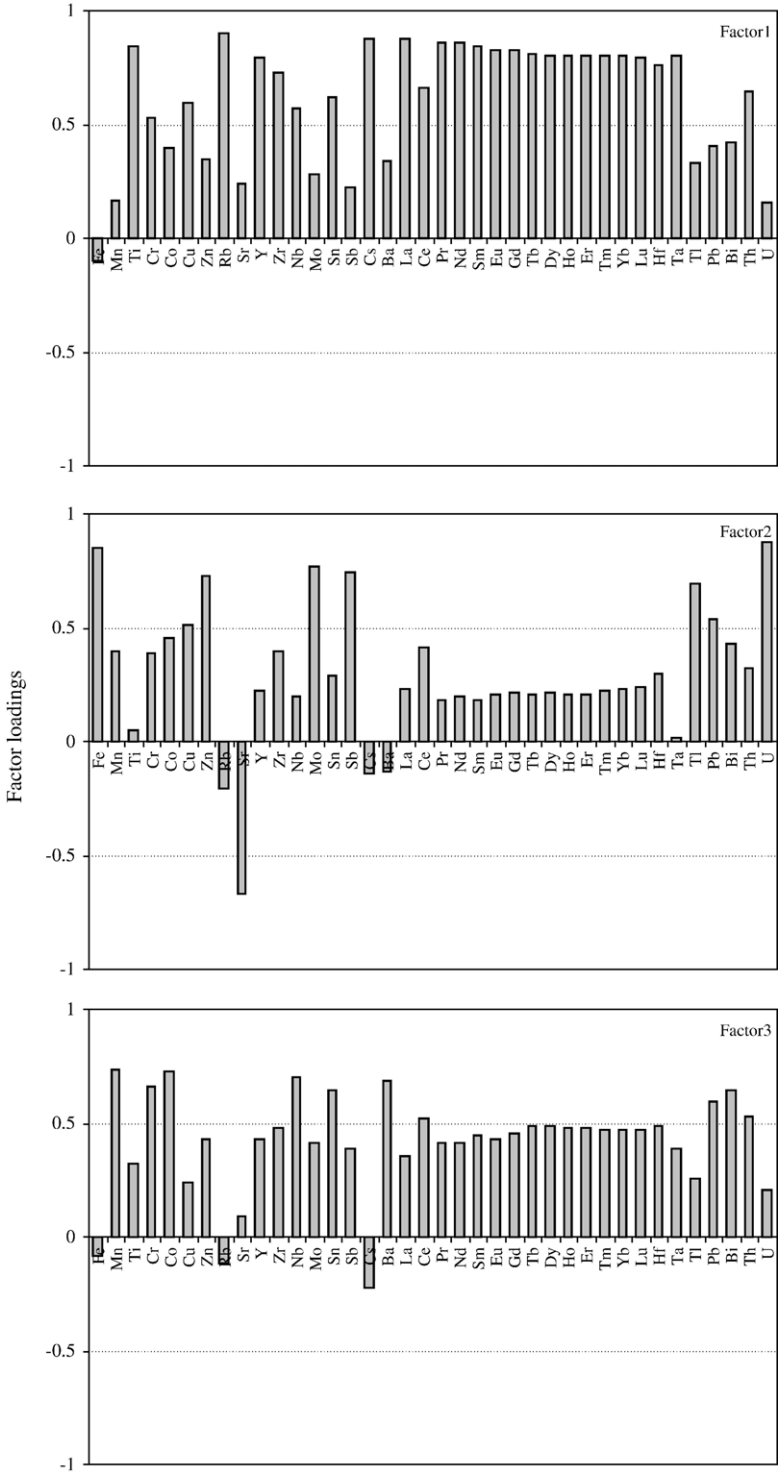

Fig. 4. PCA factor loadings for lithogenic factor (#1), Fe-phases factor (#2), and Mn-phases factor (#3) for the Kebrit crusts.

tests filled with and scattered in this high Mg-calcite matrix show no signs of dissolution, replacement or transformation (Fig. 3A). Fibrous, radial calcite constituting the tests is well preserved. These observations rule out diagenetic nature of the high Mg-calcite. The $\delta^{13}C$ values in the range of 2.4–2.9‰ for high Mg-

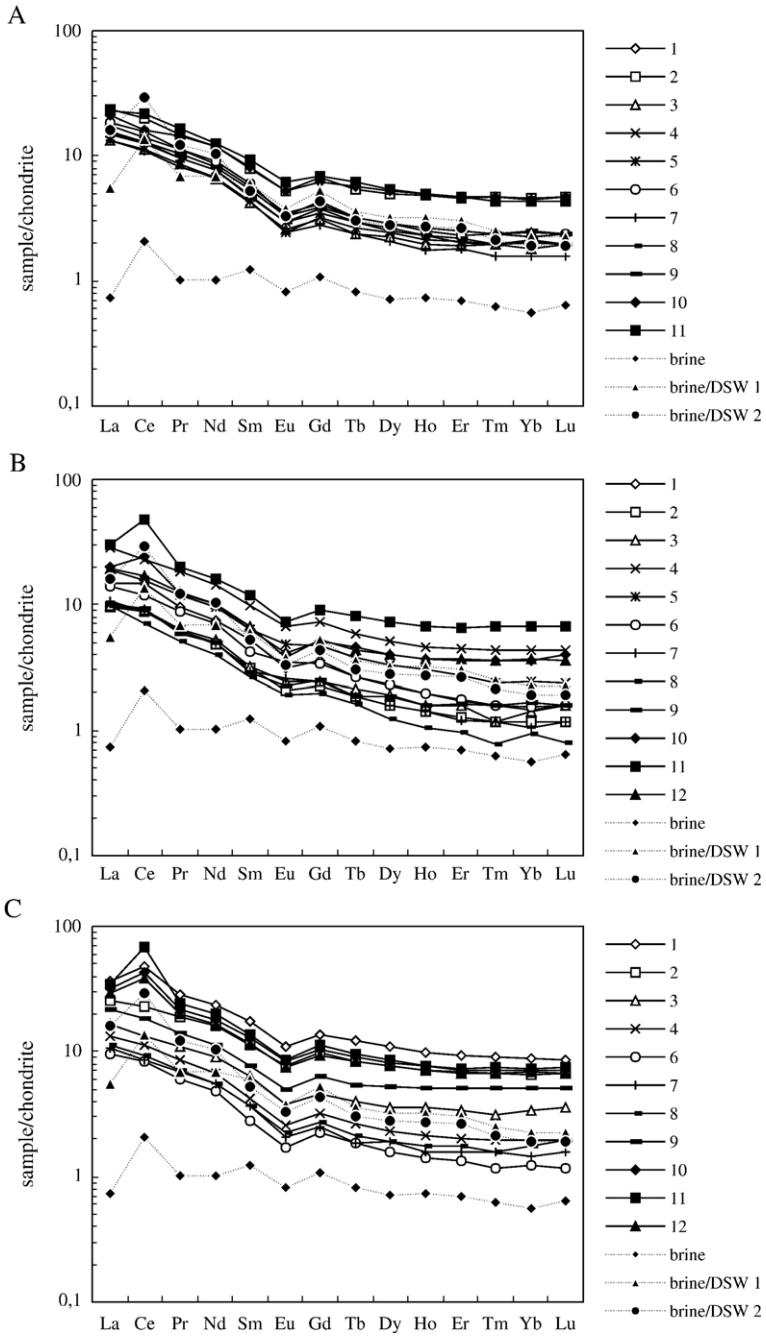

Fig. 5. C1 chondrite-normalised (Sun and McDonough, 1989) REE distribution patterns for: crust III.4 (A); crust III.5 (B); and crust VI.1 (C). Numbers in legend = layer identifications; brine/DSW 1 and 2 = lower and upper part of the transition zone between brine and deep seawater; brine and brine/DSW values $\times 10^5$.

calcite crust carbonate (Table 5) reflect mineral formation at Red Sea water temperature near isotopic equilibrium with dissolved seawater HCO_3^- in equilibrium with atmospheric CO_2 (cf. Stoffers and Botz, 1990). Based on isotope temperature calculations high Mg-calcite probably precipitated chemogenically from Red Sea water at approximately 20 °C (assuming normal Red Sea water with $\delta^{18}O = 1.8‰$ rel. SMOW).

Authigenic Mn carbonates often occur in anoxic sediments (Suess, 1979; Pedersen and Price, 1982; Jakobsen and Postma, 1989; Stoffers et al., 1990; Anschutz and Blanc, 1995; Böttcher and Huckriede,

Table 5
Isotopic compositions of the studied crusts

Type.crust.layer	Main mineral	$\delta^{13}C$ (‰)$_{PDB}$	$\delta^{18}O$ (‰)$_{PDB}$
III.4.1	Mg-calcite	2.65	1.44
III.4.3	-"-	2.90	1.42
III.4.6	-"-	2.69	1.39
III.4.9	-"-	2.37	1.18
III.5.1	Rhodochrosite	−0.95	3.10
III.5.2	-"-	−1.83	2.91

1997; Morad and Al-Aasm, 1997). The mineralogy of Mn^{2+}–Ca^{2+}–CO_3^{2-} system in marine suspended matter and sediments is thoroughly discussed elsewhere (McBride, 1979; Suess, 1979; Franklin and Morse, 1983; Morse, 1986; Wartel et al., 1990; Böttcher, 1997).

Manganese carbonate in crust III.5 might have been derived through interaction between Mn^{2+} dissolved in pore waters and marine HCO_3^-. Bacterial degradation of organic matter in the diagenetic zone of sulfate reduction could contribute CO_2. Rhodochrosite could not form in sediments overlain by anoxic water column since the degree of Mn saturation in the pore waters required for rhodochrosite precipitation can only be reached via dissolution of Mn-(hydr)oxides buried in the uppermost part of the sediment cover (Calvert and Pedersen, 1996). Such an environment can exist at the margins of anoxic basins where fluctuating redoxcline provides the necessary conditions for the precipitation of Mn-(hydr)oxides and their subsequent replacement by Mn carbonates (Hein et al., 1999). In the Kebrit Deep, Mn-(hydr)oxides precipitated in the upper section of the transition zone as well as just above it. Further redissolution of Mn-(hydr) oxides and precipitation of Mn carbonates could follow the scenario: hydrothermal activity in the deep → transgression of the transition zone upward the slope → anoxic conditions over the (hydr)oxide carpet formed above the transition zone → conversion of Mn-(hydr) oxides to Mn carbonates during early diagenesis upon a small amount of burial (e.g., Stoffers et al., 1990; Hein and Bolton, 1994; Hein et al., 1999).

Negative C isotope values (Table 5) indicate little contributions of diagenetic ^{12}C-rich carbon source to the pore waters during rhodochrosite formation. These negative $\delta^{13}C$ values (Table 5) were found in crust layers with pyrite and petroleum droplets where anoxic conditions prevail (Table 1). Bacterial sulphate reduction processes are probably responsible for the negative $\delta^{13}C$ values of rhodochrosite within those layers (Irwin et al., 1977; Pisciotto and Mahoney, 1981; and others since). This hypothesis of a diagenetic origin of rhodochrosite is confirmed by the elevated isotopic formation temperature near 30 °C, which was calculated from the $\delta^{18}O$ rhodochrosite values assuming rhodochrosite formation from (unaltered) pore water of (Red Sea) seawater origin (O'Neil et al., 1969). The homogenous, fine rhodochrosite matrix composing the rhodochrosite crust layers and filling biogenic tests (Fig. 3B) also supports the idea of diagenetic conversion of primary fine Mn-(hydr)oxides to $MnCO_3$ through interaction with marine pore-water HCO_3^- and little diagenetic CO_2. Relics of the primary precipitated Mn-(hydr)oxides not yet converted to Mn-carbonates are still preserved in the small chambers of some foraminiferal tests (Fig. 3B).

Siderite could be abiogenic, but its formation through bacterial reduction (meso-/thermophilic Fe-reducing bacteria) of amorphous Fe(III)-(hydr)oxides (e.g., Zhang et al., 1997) cannot be ruled out.

The microbial dolomite model (Vasconcelos and McKenzie, 1997; Warthmann et al., 2000) accounts well the formation of the observed accessory dolomite at relatively low temperature at the oxic/anoxic transition zone.

5.2. (Hydr)oxides

Under seawater conditions goethite is the most thermodynamically stable Fe-(hydr)oxide mineral (Glasby and Schulz, 1999) and forms under a relatively wide range of conditions (Chukhrov, 1975; Brookins, 1988). High dissolved Fe contents, relatively low O_2 concentrations and low pH (slightly acid) promote its formation (Chukhrov, 1975). Goethite formed in the presence of Mn may incorporate up to 15 mol% Mn into its structure (Stiers and Schwertmann, 1985) resulting in Mn-bearing goethite. Ferrihydrite is another widespread Fe-(hydr)oxide in natural waters (especially at the oxic/anoxic interface). It may originate from mononuclear $Fe^{3+}(OH)_i^{(3-i)}$ (Schneider and Schwyn, 1987), formed via hydrolysis and oxidation of Fe^{2+} and often occurs in marine deposits (Glasby and Schulz, 1999). Aging of ferrihydrite at pH = 4 produces goethite with traces of hematite, whereas aging at pH = 7–8 is the major pathway for hematite formation (Schwertmann and Murad, 1983).

The thin (1–7 m) transition zone between the deep seawater (oxic, slightly alkaline, cool) and Kebrit brine (anoxic, acid, warm) appears to be an important geochemical barrier and the most favorable environment for active Fe-(hydr)oxide precipitation. The dissolved Fe^{2+} meets free O_2 within the upper section of this zone and this results in rapid precipitation of primary goethite, X-ray amorphous Fe oxides (ferrihydrite), as well as Fe^{2+}/Fe^{3+} complex formation (e.g., Murray, 1979). We

suppose that lepidocrocite and hematite in the crusts are secondary minerals formed during oxidation and aging of the primary (hydr)oxide phases in neutral to alkaline conditions after the deposition. Direct abiogenic or biogenic precipitation of lepidocrocite at the transition zone cannot be ruled out (e.g., Butuzova et al., 1990).

The complex mineralogy of the crusts (Table 1) suggests formation within the fluctuating (up- and down-slope) transition zone causing gradual changes in the environmental conditions.

Chemical (autocatalytic oxidation) and microbiological processes affect the Mn geochemistry across oxic/anoxic interfaces (Kessick and Morgan, 1975; Sung and Morgan, 1981; Tebo et al., 1984; Tebo, 1991; Tebo et al., 1997). In seawater, Mn^{2+} is oxidized at much higher rates than predicted by the thermodynamic conditions of the environment (Tebo, 1991). This is explained by microbial mediation of the Mn oxidation (Tebo et al., 1997). Biologically oxic/anoxic interfaces are characterized by specific populations of bacteria that catalyze redox transformations of certain elements. Microbiota enhances significantly the rates of Mn^{2+} oxidation and maximum $Mn_{particulate}$ content is revealed just above the oxic/anoxic interfaces (Tebo et al., 1984; Tebo, 1991; Tebo et al., 1997). Mn-(hydr)oxide microbially formed at the oxic/anoxic interface in the water column of a eutrophic environment is found to be birnessite (Friedl et al., 1997).

Manganates precipitate mainly outside the Red Sea brine pools (Scholten et al., 2000). The Kebrit crust manganates, which exhibit either both 10 Å and 7 Å, or solely 7 Å characteristic basal d-spacings might (i) originate from todorokite-like low-T hydrothermal manganates; (ii) be buserite-like diagenetic minerals; or (iii) be microbially-produced buserite or/and birnessite. The transformation in air from 10 Å to 7 Å manganate could be due to insufficient structural stability (Usui et al., 1989). The trace metal content in the Kebrit crusts is relatively low and this could be the reason for structural instability of the manganates.

In the Kebrit Deep oxidation of Mn^{2+} probably starts in the upper section of the transition zone even at Eh values not high enough for abiotic oxidation, and might have elevated rates above this zone. Precipitation of poorly crystallized unstable Mn phases might have taken place in the transition zone according to the scheme: autocatalytic/bacterial oxidation of $Mn^{2+} \rightarrow$ hydration $(MnO_2 \cdot nH_2O) \rightarrow$ polymerization $(nMnO_2 \cdot mH_2O) \rightarrow$ crystallization of amorphous (hydr)oxides $\rightarrow$ transformation to poorly crystallized todorokite-like phase with a loose tunnel structure (Butuzova et al., 1990). The narrow band where this zone crossed the seafloor could contain disseminated manganates. We consider that the partially (10 Å and 7 Å) and totally (7 Å, birnessite pattern) collapsed 10 Å manganates present in the studied crusts are either diagenetic buserite-like minerals, or/and biogenic buserite/birnessite phases, rather than having originated from low-T todorokite-like hydrothermal manganates.

5.3. Sulfides

Framboidal pyrite is ubiquitous in modern anoxic environments. Its formation depends on biological activity and it can be formed in one of two fundamentally different ways: (1) biologically-induced, and (2) biologically-controlled mineralization (Bazylinski and Moskowitz, 1997). In suboxic/anoxic marine environments, SO_4^{2-} is used as an electron acceptor during the biological oxidation of organic matter and H_2S is released as a byproduct. The rate of sulfate reduction is generally at a maximum at the redoxcline (O_2/H_2S). The H_2S reacts with excess sedimentary Fe depositing Fe-sulfide minerals (Berner, 1984). A number of studies has been devoted on the low-T pyrite formation (Schoonen and Barnes, 1991a,b; Raiswell et al., 1993; Bazylinski et al., 1995; Wang and Morse, 1996; Wilkin and Barnes, 1996; Morse and Wang, 1997; Rickard and Luther, 1997; Wilkin and Barnes, 1997a; Pósfai et al., 1998; Benning et al., 2000; Butler and Rickard, 2000).

Pyrite observed in the Kebrit crusts is most abundant in layers rich in petroleum droplets (III.5, Table 1). Its formation and further preservation/transformation seems to be connected with the petroleum. Petroleum products of thermogenic origin were obviously transported upward by the ascending fluids of the fracture-controlled hydrothermal system at the flank of the Kebrit brine pool. The transition zone (acid, slightly oxygenated, microbially populated), localized at/nearby the vent field (hydrothermal petroleum emanations), contains abundant reactive Fe (dissolved, suspended, precipitated) and could be the best site for framboidal pyrite formation. Released and sedimented hydrothermal petroleum provided steep chemical gradients of rapid sulfate reduction and sulfide production around its surfaces. Eh–pH conditions in the Kebrit brine do not exclude abiogenic/biogenic onset of framboidal pyrite formation syngenetically in the water column of transition zone like in other anoxic basins (Skei, 1988; Muramoto et al., 1991; Lyons, 1997; Wilkin and Barnes, 1997b; Hurtgen et al., 1999). Moreover, the Fe-sulfides formed in the water columns of anoxic basins (Framvaren Fjord, the Black Sea, Orca Basin) showed concentration maxima just below the oxic/anoxic interface (Lyons, 1997; Cutter and Kluckhohn, 1999;

Hurtgen et al., 1999). This implies that the zone of active pyrite transfer to the underlying sediments occurs where the transition zone impinges along the margin of the deep.

Further, pyrite framboids offer nucleation surfaces for secondary (diagenetic) growth of pyrite. Consequential preservation of framboidal texture may be limited by secondary growth of pyrite that results in infilling of framboids with pyrite (Fig. 3 F), formation of porous oval pyrite (Fig. 3 B), and continued outward growth of pyrite (Fig. 3 D). Secondary growth on framboids leads to the precipitation of a sequence of different pyrite generations (Fig. 3 C, D, F) when the environmental conditions vary (Wilkin and Barnes, 1997a).

Scarce pyrite occurrences in the other crusts suggest that pyrite formation there can be closely related to microenvironmental conditions rather than bulk properties of crust layers (e.g., Jørgensen, 1977). Porewaters in the vicinity of organic matter clots or Fe-bearing minerals could be supersaturated with respect to Fe-sulfides due to localized sulfate reduction and Fe mineral dissolution (Brendel and Luther, 1995).

Γ-MnS is a low-T sedimentary authigenic mineral known from the anoxic sediments of Baltic Sea (Suess, 1979; Böttcher and Huckriede, 1997). Favorable conditions for MnS precipitation could be attained at the seawater/organic matter interface where dissolved Mn meets bacterially released H_2S. Low levels of reactive Fe are still required (Böttcher and Huckriede, 1997). Hydrothermal petroleum dispersed in some layers of crust III.5 is the best medium for γ-MnS precipitation. However, the only γ-MnS occurrence is located not in the richest in petroleum matter layer (III.5.3), which is rich in Fe minerals too, but just above it (III.5.4) in a layer with less Fe phases (Table 1).

5.4. Geochemistry

Mineralogical evidence shows that the investigated crusts formed at the seawater/brine redoxcline with extensive Mn- and Fe-(hydr)oxide precipitation. The poor correlation between Fe and Mn, and high Fe/Mn ratio (mean 24.2, range 2–261; Table 3) suggests their partitioning through the transition zone and high fractionation in the Kebrit crusts. Enrichment in Mn of the Kebrit crusts relative to the metalliferous laminae cored in the deep proper (VA-3-512; Table 3) also supports this idea.

PCA revealed several trends in the geochemistry of the crusts (Fig. 4). The terrigenous component (Factor 1) is major contributor of Rb, Cs, Zr, Hf, Ta, Y, and REE. Zinc, Mo, Sb, Tl, and U occur largely Fe-(hydr)oxide associated (Factor 2). Cobalt, Ba, and Bi are mostly connected with the Mn-phase component (Factor 3). Manganese minerals as well as terrigenous matter equally host Cr, Nb, Sn, Ce, and Th in the Kebrit crusts. Copper has a dual nature: terrigenous and Fe-phase bound. Lead is connected with the Fe- and Mn-components. Part of Co and Bi are related to the Fe-component, whereas part of Zn, Hf, Zr, Y, and HREE (Gd–Lu) are presented in the Mn-component.

As with the hydrothermal Fe–Mn crusts, the Kebrit crusts contain much less microelements (Table 3) than the hydrogenous Fe–Mn crusts from the open ocean (Hein et al., 1996, 1997; Hein and Morgan, 1999; Hein et al., 2000).

The association of microelements with the Mn- and Fe-(hydr)oxide phases in marine deposits is related to the element speciation in seawater and the physico-chemical properties of the carrier phase (Koschinsky and Halbach, 1995; Glasby and Schulz, 1999). In the Kebrit crusts the Cu_{ex}, Zn_{ex} and Co_{ex} are obviously connected with the Fe_{ex} and Mn_{ex}. Sources of Cu, Zn and Co could be both the seawater and the hydrothermal fluids. They enter the sediments through either co-precipitation with/adsorption on the Fe- and Mn-(hydr)oxides, or precipitation of sulfides. Copper and Zn are supplied in high grades by the hydrothermal systems in the open ocean, while the Co content in the hydrothermal fluids is low. However, the Cu content in the Kebrit crusts is near the BKDS values. Moreover, even the Kebrit metalliferous laminae (site VA-3-512) and massive sulfides (Blum and Puchelt, 1991) are depleted in Cu compared to other Red Sea metalliferous sediments (Scholten et al., 2000; Gurvich, 2006). If we assume hydrothermal input into the Kebrit, then Cu depletion of the fluids could be due to the interaction hydrothermal fluids/sediments: buffering of the solutions, increase in pH, decrease in T, and loss of Cu (precipitated as sulfides) beneath the seafloor. The discharge of hot hydrothermal fluids in a shallow deep like Kebrit, from the other hand, might cause boiling and phase separation (vapor + liquid) of the fluid. The cool, saline and depleted in H_2S residual liquid will supply relatively more Cu, Zn, Pb and Ba to the sediments in close vicinity of the discharge point than to the distal areas. We suppose the seawater is the only source for Cu in the crusts. A hydrothermal discharge in the central part of the deep could not account for the high Zn_{ex} of the crusts formed away on the slopes. The Co case is even more dramatic: Co in the crusts exceeds up to 2 orders of magnitude the Co content of the BKDS and central deep metalliferous laminae. High Co_{ex}, Zn_{ex} and Cu_{ex} may be explained by crust formation in the transition zone enriched in Co, Zn and Cu through a pumping mechanism operating within (e.g., Hartmann, 1985). Mn-(hydr)oxides and, less

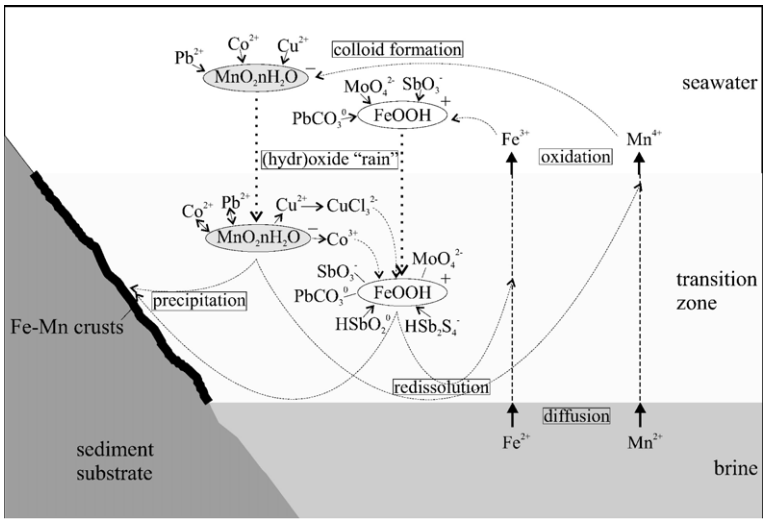

Fig. 6. Schematic model for formation of Kebrit Fe–Mn crusts illustrating Fe and Mn recycling through the transition zone and associated chemical processes.

extensively, Fe-(hydr)oxides precipitated just above the seawater/brine redoxcline (Fig. 6). Colloidal (hydr)oxide rain scavenges (co-precipitation/adsorption) Co, Zn, Cu and other trace elements from the Red Sea deep waters, sinks down through the redoxcline, dissolves back and releases the scavenged elements thus enhancing their content in the transition zone and exhausting the water layer above it. Because of their different stability fields (Glasby and Schulz, 1999), Fe-(hydr)oxides are more readily precipitated, but less readily dissolved back than Mn-(hydr)oxides in the marine environment (e.g., Crerar and Barnes, 1974).

Further, in the oxic deep water above the transition zone, Cu^{2+} is the dominant Cu species and is adsorbed on the surface of negatively charged Mn-(hydr)oxides (Fig. 6). In the transition zone Cu is released back through dissolution of the Mn-(hydr)oxides. At the lower Eh values of the transition zone dominant species of the released Cu would be $CuCl_3^{2-}$ (Glasby and Schulz, 1999). Its sorption on Mn-(hydr)oxides would be inhibited by charge considerations. Consequently, in the transition zone, Cu is attracted to the settling down clay minerals and slightly positively charged Fe-(hydr) oxides, which are resistant and hardly resolved in these conditions. This well explains the association of Cu with the terrigenous and Fe-(hydr)oxide matter (Fig. 4, Factors 1 and 2) and testifies to formation of the Kebrit crusts within the transition zone.

Co^{2+} is the principal Co aquatic species in the seawater, stable in a wide range of redox conditions (Glasby and Schulz, 1999). It may substitute for Mn^{2+} in the Mn-(hydr)oxides or be adsorbed on their negatively charged surfaces. Oxidation of Co^{2+} incorporated in the manganates by Mn^{4+} results in Co^{3+}. Co^{3+} could be incorporated in the Fe-(hydr)oxides substituting for Fe^{3+}, but could not be adsorbed on their positively charged surfaces. In the slightly oxic to reduced Kebrit transition zone Co^{3+}, released through the dissolution of the Mn-(hydr)oxides, would be less stable with respect to Co^{2+}. Hence, Co^{2+} would be the principal Co species in this zone too. This explains the higher association of Co with Mn^{2+}-phases ((hydr)oxides, carbonates) than the Fe-phase (Fe^{3+}) and terrigenous carriers (Fig. 4).

Pb^{2+} and $PbCO_3^0$ are the principal Pb aquatic species in the seawater. Pb^{2+} is attracted to the negatively charged Mn-(hydr)oxides, while the large $PbCO_3^0$ complex with low charge density is attracted to the positive charge of the Fe-(hydr)oxide surfaces (Fig. 6). This accounts for almost equal distribution of Pb with both the Fe- and Mn-phases (Fig. 4).

Antimony, Mo and U are sensitive to changes in redox conditions. Precipitation and redissolution reactions across the transition zone lead to considerable changes in the distribution of these elements between soluble and particulate forms. The Sb and Mo contents in particulate matter sharply increase at the oxic/anoxic interface and then rapidly decrease in the brine towards the sediments (Van der Sloot et al., 1990). The change in chemical speciation of Sb at the transition zone, where predominantly pentavalent Sb (SbO_3^-) present in the oxygenated deep seawater will be reduced to trivalent Sb ($HSbO_2^0$, $HSb_2S_4^-$) in the oxic/anoxic transition zone (Spycher and Reed, 1989), causes adsorption or precipitation reactions of the reduced species onto the

suspended matter. These Sb species are mainly attracted by the slightly positively charged Fe-(hydr)oxides (Fig. 6), which explains the association of Sb with the Fe-rich phases (Fig. 4; Factor 2). The abrupt drop in the suspended Sb content in the brine (Van der Sloot et al., 1990) could be due to two reasons: (1) redissolution of the scavenged Sb under the anoxic conditions; (2) the seawater/brine redoxcline acts as a sieve, not allowing the passage of fine Sb-enriched suspended phases with an effective density greater than that of the brine. The Sb content of the Kebrit crusts, 1–2 orders of magnitude higher than that of the BKDS (Table 3), suggests again for the crust formation at the seawater/brine redoxcline.

The main Mo species dissolved in the seawater is MoO_4^{2-}. This large negatively charged complex is readily scavenged by Fe-(hydr)oxides (Fig. 6). That is why Mo appears associated mainly with the Fe-component (Fig. 4). It has been established (Crusius et al., 1996) that Mo accumulates substantially in sediments underlying waters with free H_2S (e.g., Black Sea, Saanich Inlet, Cariaco Basin, Framvaren fjord). However, these enrichments rarely exceed 100 ppm (usually 20–40 ppm). Sulfidic waters of the Kebrit brine could hardly provide conditions for authigenic Mo accumulation as high as to exceed concentrations of 100 ppm in the sediments. The Kebrit crust layers with the highest Mo contents (Mo > 120 ppm; Table 3) probably did not form in either the reduced brine or in the oxygenated Red Sea deep waters. The intersection of the transition zone (where particulate Mo reaches maximum value) with the seafloor seems to be the most possible place of formation of the crust layers with the highest Mo contents. This further supports our suggestion that the studied crusts formed in the transition zone. Layers enriched in Mo (10–100 ppm) formed in the presence of free H_2S in the lower reduced section of the transition zone. Significant enrichment (> 100 ppm) implies deposition at this zone. The vertical distribution of this sensitive geochemical tracer across the crusts (Table 3) suggests vertical fluctuations of the Kebrit transition zone.

It could be expected that the background terrigenous suspension would be diluted in the Kebrit transition zone by the high (hydr)oxide suspended matter content. Consequently, the contents of elements with terrigenous nature such as Th, La, Ce, Sm, and Hf in the sediments where the transition zone crosses the deep walls will be lower than those of the BKDS. Concentrations of these elements in the Kebrit crusts (Table 3) are further evidence that these crusts have formed at the transition zone.

The distributions of the REE across the oxic/anoxic interfaces have been studied at various basins (de Baar et al., 1988; German et al., 1991) and are similar to the ones recorded here. In our investigation, we used for comparison the REE patterns in the eastern Mediterranean anoxic hypersaline Bannock (Schijf et al., 1995) and Tyro (Bau et al., 1997) basins, since their genesis was similar to that of the Kebrit Deep. Yttrium and REE are involved in the redox-cycling of Mn and Fe through the oxic/anoxic interfaces (de Baar et al., 1988; German et al., 1991; Schijf et al., 1995; Bau et al., 1997). Precipitation of Mn- and Fe-(hydr)oxides above the redox cline, scavenging of REE, further dissolution of the (hydr)oxides below the redox boundary and liberation of the REE generates REE distribution patterns of the anoxic waters, which differ from that of the overlying seawater: (1) large negative Ce anomaly of the oxic deep seawater transforms into smaller negative even positive Ce anomaly of the anoxic waters; (2) less fractionation of the LREE and HREE in the anoxic than in the overlying seawater.

The REE patterns with no Ce anomaly of the Kebrit crusts resemble much that of the post-Archean Australian shales and upper continental crust (McLennan, 1989). However, the low absolute abundances of the terrigenous component and REEs (ΣREE; Table 3) in the Kebrit crusts exclude significant terrigenous imprint on the patterns. The low REE values imply for a hydrothermal genesis (e.g., Hein et al., 1997), but the low-T hydrothermal deposits exhibit strong negative Ce anomaly (Usui et al., 1997). Kebrit crusts have REE patterns similar to those of the oceanic diagenetic Fe–Mn (hydr)oxide crusts (Usui et al., 1997), but contain 1–2 orders of magnitude less REE and Y than diagenetic crusts (Hein et al., 1997, 2000). Some of the Kebrit crusts REE patterns are similar to those of the Kebrit brine and transition zone with positive Ce and negative Eu anomalies (Fig. 5), which supports the other geochemical and mineralogical evidence for formation of the crusts in the transition zone. Alternation of layers with positive–no-positive Ce anomaly (Fig. 5B,C) suggests crust formation at the fluctuating transition zone.

6. Conclusions

(1) The lithified sediment layers recovered from the Kebrit Deep have complex mineralogy: Fe- and Mn-(hydr)oxides, carbonates and sulfides.
(2) Mineralogical and geochemical features of these layers indicate formation in the sediment where the transition zone between the oxic deep seawater and anoxic Kebrit Deep brine crosses the seafloor.
(3) Primary Fe and Mn enrichment through recycling in the transition zone, is the result of hydrothermal

activity in the deep. Their precipitation (abiogenic/biogenic) superimposed the chemogenic carbonate precipitation resulted in the formation of lithified metalliferous layers.

(4) The cyclic Fe- and Mn-(hydr)oxide precipitation/redissolution through the redoxcline pumps a number of elements from the deep seawater into the brine and produces their enrichment in the underlying sediments.

(5) The carbonates cementing the Fe–Mn-(hydr) oxides formed from normal saline seawater at temperatures between 20° and 30 °C.

(6) Diagenetic processes lead to formation of rhodochrosite, dolomite, siderite, mixed carbonates and pyrite.

Acknowledgements

Many thanks go to: J. Hein (USGS), J. Milliman (College of William and Mary, USA) and A. Usui (GSJ) who provided insightful comments on a preliminary draft of this manuscript; M. Hartmann (University of Kiel, Germany), G. Cutter (Old Dominion University, USA) and J. Morse (Texas A&M University, USA) for very fruitful discussions; H. Elderfield (University of Cambridge, UK), E. Sholkovitz (WHOI, USA), P. Halbach (Freie Universität Berlin, Germany), H. Barnes (Pennsylvania State University, USA), T. Lyons (University of Missouri, USA), D. Blowes (University of Waterloo, Canada), P. Anschutz (Université Bordeaux, France), D. Cronan (ICST, UK) and D. Rickard (Cardiff University, UK) who sent much valuable literature. This manuscript was significantly improved by comments and suggestions made by G.J. De Lange and the two anonymous reviewers. V.M. Dekov was supported through a postdoctoral fellowship from the German Service for Academic Exchange (DAAD), which is much appreciated. This study was supported by the Deutsche Forschungsgemeinschaft (Sto110/23-5).

References

Anschutz, P., Blanc, G., 1995. Diagenetic evolution of the DOP facies from the Atlantis II Deep (Red Sea): evidence of early hydrothermal activity. Oceanol. Acta 18, 105–112.

Bäcker, H., Richter, H., 1973. Die rezente hydrothermal-sedimentäre Lagerstätte Atlantis-II-Tief im Roten Meer. Geol. Rundsch. 62, 697–741.

Bau, M., Möller, P., Dulski, P., 1997. Yttrium and lanthanides in eastern Mediterranean seawater and their fractionation during redox-cycling. Mar. Chem. 56, 123–131.

Bazylinski, D.A., Moskowitz, B.M., 1997. Microbial biomineralization of magnetic iron minerals: microbiology, magnetism and environmental significance. Rev. Mineral. 35, 181–223.

Bazylinski, D.A., Frankel, R.B., Heywood, B.R., Mann, S., King, J.W., Donaghay, P.L., Hanson, A.K., 1995. Controlled biomineralization of magnetite (Fe_3O_4) and greigite (Fe_3S_4) in a magnetotactic bacterium. Appl. Environ. Microbiol. 61, 3232–3239.

Benning, L.G., Wilkin, R.T., Barnes, H.L., 2000. Reaction pathways in the Fe–S system below 100 °C. Chem. Geol. 167, 25–51.

Berner, R.A., 1984. Sedimentary pyrite formation: an update. Geochim. Cosmochim. Acta 48, 605–615.

Bignell, R.D., 1975. The Geochemistry of Metalliferous Brine Precipitates and Other Sediments in the Red Sea. Ph.D. thesis, University of London, 276 pp.

Bignell, R.D., Cronan, D.S., Tooms, J.S., 1976. Red Sea metalliferous brine precipitates. Geol. Assoc. Can. Spec. Pap. 14, 147–184.

Blum, N., Puchelt, H., 1991. Sedimentary-hosted polymetallic massive sulfide deposits of the Kebrit and Shaban Deeps, Red Sea. Miner. Depos. 26, 217–227.

Bonatti, E., 1985. Punctiform initiation of sea floor spreading in the Red Sea during transition from a continent to an oceanic rift. Nature 316, 33–37.

Bonatti, E., 1987. The rifting of continents. Sci. Am. 256, 75–81.

Bonatti, E., Seyler, M., 1987. Crustal underplating and evolution in the Red Sea rift: uplifted gabbro/gneiss crustal complex on Zarbargad and Brothers Islands. J. Geophys. Res. 92, 12803–12821.

Böttcher, M.E., 1997. The transformation of aragonite to $Mn_xCa_{(1-x)}CO_3$ solid-solutions at 20 °C: an experimental study. Mar. Chem. 57, 97–106.

Böttcher, M.E., Huckriede, H., 1997. First occurrence and stable isotope composition of authigenic γ-MnS in the central Gotland Deep (Baltic Sea). Mar. Geol. 137, 201–205.

Brendel, P.J., Luther III, G.W., 1995. Development of a gold amalgam volumetric microelectrode for the determination of dissolved Fe, Mn, O_2 and S(-II) in porewaters of marine and freshwater sediments. Environ. Sci. Technol. 29, 751–761.

Brookins, D.G., 1988. Eh–pH Diagrams for Geochemistry. Springer, Berlin. 176 pp.

Butler, I.B., Rickard, D., 2000. Framboidal pyrite formation via the oxidation of iron (II) monosulfide by hydrogen sulfide. Geochim. Cosmochim. Acta 64, 2665–2672.

Butuzova, G.Yu., Drits, V.A., Morozov, A.A., Gorschkov, A.I., 1990. Processes of formation of iron–manganese oxyhydroxides in the Atlantis-II and Thetis Deeps of the Red Sea. Spec. Publ. Int. Assoc. Sedimentol. 11, 57–72.

Calvert, S.E., Pedersen, T.F., 1996. Sedimentary geochemistry of manganese: implications for the environment of formation of manganiferous black shales. Econ. Geol. 91, 36–47.

Chukhrov, F.V. (Ed.), 1975. Hypergenic Iron Oxides in Geological Processes. Nauka, Moscow. 207 pp. (in Russian).

Crerar, D.A., Barnes, H.L., 1974. Deposition of deep-sea manganese nodules. Geochim. Cosmochim. Acta 38, 279–300.

Crusius, J., Calvert, S., Pedersen, T., Sage, D., 1996. Rhenium and molybdenum enrichments in sediments as indicators of oxic, suboxic and sulfidic conditions of deposition. Earth Planet. Sci. Lett. 145, 65–78.

Cutter, G.A., Kluckhohn, R.S., 1999. The cycling of particulate carbon, nitrogen, sulfur, and sulfur species (iron monosulfide, greigite, pyrite, and organic sulfur) in the water columns of Framvaren Fjord and the Black Sea. Mar. Chem. 67, 149–160.

de Baar, H.J.W., German, C.R., Elderfield, H., van Gaans, P., 1988. Rare earth element distributions in anoxic waters of the Cariacho Trench. Geochim. Cosmochim. Acta 52, 1203–1219.

Degens, E.T., Ross, D.A., 1969. Hot Brines and Recent Heavy Metal Deposits in the Red Sea. Springer, New York. 600 pp.

De Lange, G.J., Catalano, G., Klinkhammer, G.P., Luther III, G.W., 1990a. The interface between oxic seawater and the anoxic Bannock brine; its sharpness and the consequences for the redox-related cycling of Mn and Ba. Mar. Chem. 31, 205–217.

De Lange, G.J., Middelburg, J.J., Van der Weijden, C.H., Catalano, G., Luther III, G.W., Hydes, D.J., Woittiez, J.R.W., Klinkhammer, G.P., 1990b. Composition of anoxic hypersaline brines in the Tyro and Bannock Basins, eastern Mediterranean. Mar. Chem. 31, 63–88.

Emerson, S., Cranston, R.E., Liss, P.S., 1979. Redox species in a reducing fjord: equilibrium and kinetic considerations. Deep-Sea Res. 26 A, 859–879.

Franklin, M.L., Morse, J.W., 1983. The interaction of manganese (II) with the surface of calcite in dilute solutions and seawater. Mar. Chem. 12, 241–254.

Friedl, G., Wehrli, B., Manceau, A., 1997. Solid phases in the cycling of manganese in eutrophic lakes: new insights from EXAFS spectroscopy. Geochim. Cosmochim. Acta 61, 275–290.

Galimov, E.M., Kodina, L.A., Bogacheva, M.P., Vlassova, L.N., 1995. Nature of organic matter of hydrothermal sulfide ores and sediments of the Kebrit Deep, Red Sea. Geokhimiya 8, 1178–1190 (in Russian).

Garbe-Schönberg, C.-D., 1993. Simultaneous determination of thirty seven trace elements in twenty eight international rock standards by ICP-MS. Geostand. Newsl. 17, 81–97.

German, C.R., Holliday, B.P., Elderfield, H., 1991. Redox cycling of rare earth elements in the suboxic zone of the Black Sea. Geochim. Cosmochim. Acta 55, 3553–3558.

Gevirtz, J.L., Friedman, G.M., 1966. Deep-sea carbonate sediments of the Red Sea and their implications on marine lithification. J. Sediment. Petrol. 36, 143–152.

Glasby, G.P., Schulz, H.D., 1999. Eh, pH diagrams for Mn, Fe, Co, Ni, Cu and As under seawater conditions: application of two new types of Eh, pH diagrams to the study of specific problems in marine geochemistry. Aquat. Geochem. 5, 227–248.

Gurvich, E.G., 2006. Metalliferous Sediments of the World Ocean. Fundamental Theory of Deep-Sea Hydrothermal Sedimentation. Springer, Heidelberg. p. 416.

Hartmann, M., 1985. Atlantis-II Deep geothermal brine system. Chemical processes between hydrothermal brines and Red Sea deep water. Mar. Geol. 64, 157–177.

Hartmann, M., Scholten, J.C., Stoffers, P., Wehner, F., 1998. Hydrographic structure of brine-filled deeps in the Red Sea — new results from the Shaban, Kebrit, Atlantis II, and Discovery Deep. Mar. Geol. 144, 311–330.

Hein, J.R., Bolton, B., 1994. Formation of the Chiatura and Nikopol manganese carbonate ores, Georgia and Ukraine. Abstracts, Fermor Lecture Meeting. The Geological Society of London, London, England, p. 12. 26–27. September.

Hein, J.R., Morgan, C.L., 1999. Influence of substrate rocks on Fe–Mn crust composition. Deep-Sea Res. I 46, 855–875.

Hein, J.R., Gibbs, A.E., Clague, D.A., Torresan, M., 1996. Hydrothermal mineralization along submarine rift zones, Hawaii. Mar. Georesour. Geotechnol. 14, 177–203.

Hein, J.R., Koschinsky, A., Halbach, P., Manheim, F.T., Bau, M., Kang, J.-K., Lubick, N., 1997. Iron and manganese oxide mineralization in the Pacific. In: Nicholson, K., Hein, J.R., Bühn, B., Dasgupta, S. (Eds.), Manganese Mineralization: Geochemistry and Mineralogy of Terrestrial and Marine Deposits. Geological Society Special Publication, vol. 119, pp. 123–138.

Hein, J.R., Fan, D., Ye, J., Liu, T., Yeh, H.-W., 1999. Composition and origin of Early Cambrian Tiantaishan phosphorite–Mn carbonate ores, Shaanxi Province, China. Ore Geol. Rev. 15, 95–134.

Hein, J.R., Koschinsky, A., Bau, M., Manheim, F.T., Kang, J.-K., Roberts, L., 2000. Cobalt-rich ferromanganese crusts in the Pacific. In: Cronan, D.S. (Ed.), Handbook of Marine Mineral Deposits. CRC Press, Boca Raton, pp. 239–279.

Hemleben, Ch., Roether, W., Stoffers, P., 1996. Östliches Mittelmeer, Rotes Meer, Arabisches Meer, Cruise No. 31, 30 December 1994–22 March 1995. Meteor Berichte, vol. 96-4. Universität Hamburg. 282 pp.

Herman, Y.R., 1965. Études des sédiments Quaternaires de la Mer Rouge. Ph.D. thesis, Université de Paris, Masson and Cie, Paris, 339 pp.

Hurtgen, M.T., Lyons, T.W., Ingall, E.D., Cruse, A.M., 1999. Anomalous enrichments of iron monosulfide in euxinic marine sediments and the role of H_2S in iron sulfide transformations: examples from Effingham Inlet, Orca Basin, and the Black Sea. Am. J. Sci. 299, 556–588.

Irwin, H., Curtis, C., Coleman, M., 1977. Isotopic evidence for source of diagenetic carbonates formed during burial of organic-rich sediments. Nature 269, 209–213.

Izzeldin, Y.A., 1987. Seismic, gravity and magnetic surveys in the central part of the Red Sea: their interpretation and implications for the structure and evolution of the Red Sea. Tectonophysics 143, 269–306.

Jakobsen, R., Postma, D., 1989. Formation and solid solution behavior of Ca-rhodochrosites in marine muds of the Baltic deeps. Geochim. Cosmochim. Acta 53, 2639–2648.

Jørgensen, B.B., 1977. Bacterial sulfate reduction within reduced microniches of oxidized marine sediments. Mar. Biol. 41, 7–17.

Kessick, M.A., Morgan, J.J., 1975. Mechanism of auto-oxidation of manganese in aqueous solution. Environ. Sci. Technol. 9, 157–159.

Koschinsky, A., Halbach, P., 1995. Sequential leaching of marine ferromanganese precipitates: genetic implications. Geochim. Cosmochim. Acta 59, 5113–5132.

Le Pichon, X., Gaullier, J.M., 1988. The rotation of the Arabia and Levant Fault System. Tectonophysics 153, 271–294.

Lissitzyn, A.P., Bogdanov, Yu.A., 1986. Metalliferous Sediments of Red Sea. Nauka, Moscow. 288 pp. (in Russian).

Lyons, T.W., 1997. Sulfur isotopic trends and pathways of iron sulfide formation in upper Holocene sediments of the anoxic Black Sea. Geochim. Cosmochim. Acta 61, 3367–3382.

Makris, J., Rihm, R., 1991. Shear-controlled evolution of the Red Sea: pull apart model. Tectonophysics 198, 441–466.

McBride, M.B., 1979. Chemisorption and precipitation of Mn^{2+} at $CaCO_3$ surfaces. Soil Sci. Soc. Am. J. 43, 693–698.

McCrea, J.M., 1950. The isotope chemistry of carbonates and a paleotemperature scale. J. Chem. Phys. 18, 849–857.

McLennan, S.M., 1989. Rare earth elements in sedimentary rocks: influence of provenance and sedimentary processes. In: Lipin, B. R., McKay, G.A. (Eds.), Geochemistry and Mineralogy of Rare Earth Elements. Rev. Miner., vol. 21, pp. 169–200.

Michaelis, W., Jenisch, A., Richnow, H.H., 1990. Hydrothermal petroleum generation in Red Sea sediments from the Kebrit and Shaban Deeps. Appl. Geochem. 5, 103–114.

Milliman, J.D., 1974. Marine Carbonates. Springer, Berlin. 375 pp.

Milliman, J.D., Ross, D.A., Ku, T.-L., 1969. Precipitation and lithification of deep-sea carbonates in the Red Sea. J. Sediment. Petrol. 39, 724–736.

Missack, E.A., 1988. Mineralogy and phase relations of the massive sulphides and metalliferous sediments of the Axial Rift Valley, Red Sea. Heidelb. Geowiss. Abh. 23, 211 pp.

Morad, S., Al-Aasm, I.S., 1997. Conditions of rhodochrosite-nodule formation in Neogene–Pleistocene deep-sea sediments: evidence from O, C and Sr isotopes. Sediment. Geol. 114, 295–304.

Morse, J.W., 1986. The surface chemistry of calcium carbonate minerals in natural waters: an overview. Mar. Chem. 20, 91–112.

Morse, J.W., Wang, Q., 1997. Pyrite formation under conditions approximating those in anoxic sediments. II. Influence of precursor iron minerals and organic matter. Mar. Chem. 57, 187–193.

Müller, G., Gastner, M., 1971. The carbonate bombe, a simple device for the determination of the carbonate content in sediments, soils and other materials. Neues Jahrb. Mineral. 10, 466–469.

Muramoto, J.A., Honjo, S., Fry, B., Hay, B.J., Howarth, R.W., Cisne, J. L., 1991. Sulfur, iron and organic carbon fluxes in the Black Sea: sulfur isotopic evidence for origin of sulfur fluxes. Deep-Sea Res. 38, S1151–S1187.

Murray, J.W., 1979. Iron oxides. In: Burns, R.G. (Ed.), Marine Minerals. Min. Soc. Am., Rev. Mineral., 6. 47–98.

Natterer, K., 1898. Expedition S.M. Schiff "Pola" in das Rote Meer Nördliche Hälfte (Oktober 1895–May 1896). Denkschr. - Akad. Wiss. Wien, Math.-Nat. 65, 445–572.

Olauson, E., 1960. Description of sediment cores from the Mediterranean and Red Sea. Rep. Swed. Deep-Sea Exped., 1947-1948 8, 287–334.

O'Neil, J.R., Clayton, R.N., Mayeda, T.K., 1969. Oxygen isotope fractionation in divalent metal carbonates. J. Chem. Phys. 51, 5547–5558.

Pedersen, T.F., Price, N.B., 1982. The geochemistry of manganese carbonate in Panama Basin sediments. Geochim. Cosmochim. Acta 46, 59–68.

Pisciotto, K.A., Mahoney, J.J., 1981. Isotopic survey of diagenetic carbonates, Deep Sea Drilling Project Leg 63. In: Yeats, R.S., Haq, B.U., et al. (Eds.), Init. Rep. DSDP, vol. 63, pp. 595–609.

Pósfai, M., Buseck, P.R., Bazylinski, D.A., Frankel, R.B., 1998. Reaction sequence of iron sulfide minerals in bacteria and their use as biomarkers. Science 280, 880–883.

Raiswell, R., Whaler, K., Dean, S., Coleman, M.L., Briggs, D.E.G., 1993. A simple three-dimensional model of diffusion-with-precipitation applied to localized pyrite formation in framboids, fossils and detrital iron minerals. Mar. Geol. 113, 89–100.

Rickard, D., Luther III, G.W., 1997. Kinetics of pyrite formation by the H_2S oxidation of iron (II) monosulphide in aqueous solutions between 25 °C and 125 °C: the mechanism. Geochim. Cosmochim. Acta 61, 135–147.

Schijf, J., de Baar, H.J.W., Millero, F.J., 1995. Vertical distributions and speciation of dissolved rare earth elements in the anoxic brines of the Bannock Basin, eastern Mediterranean Sea. Geochim. Cosmochim. Acta 59, 3285–3299.

Schmidt, M., Botz, R., Faber, E., Schmitt, M., Poggenburg, J., Garbe-Schönberg, D., Stoffers, P., 2003. High-resolution methane profiles across anoxic brine–seawater boundaries in the Atlantis-II, Discovery, and Kebrit Deeps (Red Sea). Chem. Geol. 200, 359–375.

Schneider, W., Schwyn, B., 1987. The hydrolysis of iron in synthetic, biological, and aquatic media. In: Stumm, W. (Ed.), Aquatic Surface Chemistry. Wiley, New York, pp. 167–196.

Schoell, M., 1974. Valdivia VA 01/03, Hydrographie II und III. Bundesanst. Bodenforschung, Hannover. 1063 pp.

Scholten, J.C., Stoffers, P., Garbe-Schönberg, D., Moammar, M., 2000. Hydrothermal mineralization in the Red Sea. In: Cronan, D. S. (Ed.), Handbook of Marine Mineral Deposits. CRC Press, Boca Raton, pp. 369–395.

Schoonen, M.A.A., Barnes, H.L., 1991a. Reactions forming pyrite: I. Nucleation of FeS_2 below 100 °C. Geochim. Cosmochim. Acta 55, 1495–1504.

Schoonen, M.A.A., Barnes, H.L., 1991b. Reactions forming pyrite and marcasite from solution: II. Via FeS precursors below 100 °C. Geochim. Cosmochim. Acta 55, 1505–1514.

Schwertmann, U., Murad, E., 1983. Effect of pH on the formation of goethite and hematite from ferrihydrite. Clay Clay Miner. 31, 277–284.

Skei, J.M., 1988. Formation of framboidal iron sulfide in the water of a permanently anoxic fjord — Framvaren, South Norway. Mar. Chem. 23, 345–352.

Spencer, D.W., Brewer, P.G., 1971. Vertical advective diffusion and redox potentials as controls in the distribution of manganese and other trace metals dissolved in waters of the Black Sea. J. Geophys. Res. 76, 5877–5892.

Spycher, N.F., Reed, M.H., 1989. As (III) and Sb (III) sulfide complexes: an evaluation of stoichiometry and stability from existing experimental data. Geochim. Cosmochim. Acta 53, 2185–2194.

Stiers, W., Schwertmann, U., 1985. Evidence for manganese substitution in synthetic goethite. Geochim. Cosmochim. Acta 49, 1909–1911.

Stoffers, P., Botz, R., 1990. Carbonate crusts in the Red Sea: their composition and isotope geochemistry. In: Ittekkot, V., Kempe, S., Michaelis, W., Spitzy, A. (Eds.), Facets of Modern Biogeochemistry. Springer, Berlin, pp. 242–252.

Stoffers, P., Botz, R., Scholten, J., 1990. Isotope geochemistry of primary and secondary carbonate minerals in the Shaban-Deep (Red Sea). In: Heling, D., Rothe, P., Förstner, U., Stoffers, P. (Eds.), Sediments and Environmental Geochemistry. Springer, Berlin, pp. 83–94.

Suess, E., 1979. Mineral phases formed in anoxic sediments by microbial decomposition of organic matter. Geochim. Cosmochim. Acta 43, 339–352.

Sun, S.-S., McDonough, W.F., 1989. Chemical and isotopic systematics of oceanic basalts: implications for mantle composition and processes. In: Saunders, A.D., Norry, M.J. (Eds.), Geol. Soc. London, Spec. Publ., vol. 42, pp. 313–345.

Sung, W., Morgan, J.J., 1981. Oxidative removal of Mn(II) from solution catalyzed by the γ-FeOOH (lepidocrocite) surface. Geochim. Cosmochim. Acta 45, 2377–2383.

Tebo, B.M., 1991. Manganese (II) oxidation in the suboxic zone of the Black Sea. Deep-Sea Res 38, S883–S905.

Tebo, B.M., Nealson, K.H., Emerson, S., Jacobs, L., 1984. Microbial mediation of Mn(II) and Co(II) precipitation at the O_2/H_2S interfaces in two anoxic fjords. Limnol. Oceanogr. 29, 1247–1258.

Tebo, B.M., Ghiorse, W.C., van Waasbergen, L.G., Siering, P.L., Caspi, R., 1997. Bacterially mediated mineral formation; insights into manganese (II) oxidation from molecular genetic and biochemical studies. Rev. Miner. 35, 225–266.

Usui, A., Mellin, T.A., Nohara, M., Yuasa, M., 1989. Structural stability of marine 10 Å manganates from the Ogasawara (Bonin) arc: implication for low-temperature hydrothermal activity. Mar. Geol. 86, 41–56.

Usui, A., Bau, M., Yamazaki, T., 1997. Manganese microchimneys buried in the Central Pacific pelagic sediments: evidence of intraplate water circulation? Mar. Geol. 141, 269–285.

Van der Sloot, H.A., Hoede, D., Hamburg, G., Woittiez, J.R.W., Van der Weijden, C.H., 1990. Trace elements in suspended matter from the anoxic hypersaline Tyro and Bannock Basins (eastern Mediterranean). Mar. Chem. 31, 187–203.

Vasconcelos, C., McKenzie, J.A., 1997. Microbial mediation of modern dolomite precipitation and diagenesis under anoxic conditions (Lagoa Vermelha, Rio de Janeiro, Brasil). J. Sed. Res. 67, 378–390.

Veber, V.V., Gurskiy, Yu.N., 1982. Malt formation in the recent sediments of the Kebrit brine pool, Red Sea. Geol. Oil Gas 1, 29–33 (in Russian).

Wang, Q., Morse, J.W., 1996. Pyrite formation under conditions approximating those in anoxic sediments. I. Pathway and morphology. Mar. Chem. 52, 99–121.

Wartel, M., Skiker, M., Auger, Y., Boughriet, A., 1990. Interaction of manganese (II) with carbonates in seawater: assessment of the solubility product of $MnCO_3$ and Mn distribution coefficient between the liquid phase and $CaCO_3$ particles. Mar. Chem. 29, 99–117.

Warthmann, R., van Lith, Y., Vasconcelos, C., McKenzie, J.A., Karpoff, A.-M., 2000. Bacterially induced dolomite precipitation in anoxic culture experiments. Geology 28, 1091–1094.

Wedepohl, K.H., 1971. Environmental influences on the chemical composition of shales and clays. In: Ahrens, L.H., Press, F., Runcorn, S.K., Urey, H.C. (Eds.), Physics and Chemistry of the Earth. Pergamon, Oxford, pp. 307–331.

Wilkin, R.T., Barnes, H.L., 1996. Pyrite formation by reactions of iron monosulfides with dissolved inorganic and organic sulfur species. Geochim. Cosmochim. Acta 60, 4167–4179.

Wilkin, R.T., Barnes, H.L., 1997a. Formation processes of framboidal pyrite. Geochim. Cosmochim. Acta 61, 323–339.

Wilkin, R.T., Barnes, H.L., 1997b. Pyrite formation in an anoxic estuarine basin. Am. J. Sci. 297, 620–650.

Zhang, C., Liu, S., Phelps, T.J., Cole, D.R., Horita, J., Fortier, S.M., Elless, M., Valley, J.W., 1997. Physiochemical, mineralogical, and isotopic characterization of magnetite-rich iron oxides formed by thermophilic iron-reducing bacteria. Geochim. Cosmochim. Acta 61, 4621–4632.